Rooze, J., Zeller, M. A., Gogina, M., Roeser, P., Kallmeyer, J., Schönke, M., Radtke, H., Böttcher, M. E. (2024): Bottom-trawling signals lost in sediment: A combined biogeochemical and modeling approach to early diagenesis in a perturbed coastal area of the southern Baltic Sea. - Science of the Total Environment, 906, 167551.

https://doi.org/10.1016/j.scitotenv.2023.167551

Bottom-trawling signals lost in sediment: A combined biogeochemical and modeling approach to early diagenesis in a perturbed coastal area of the southern Baltic Sea

Jurjen Rooze[a,b,*], Mary A. Zeller[b,1], Mayya Gogina[c], Patricia Roeser[b,2], Jens Kallmeyer[d], Mischa Schönke[e], Hagen Radtke[a], Michael Ernst Böttcher[b,e,f]

[a]Department of Physical Oceanography and Instrumentation, Leibniz Institute for Baltic Sea Research Warnemünde (IOW), 18119 Rostock, Germany
[b]Department of Marine Geology, Leibniz Institute for Baltic Sea Research Warnemünde (IOW), 18119 Rostock, Germany
[c]Biological Oceanography, Leibniz Institute for Baltic Sea Research Warnemünde (IOW), 18119 Rostock, Germany
[d]Geomicrobiology, GFZ German Research Center for Geosciences, 14473 Potsdam, Germany
[e]Marine Geochemistry, University of Greifswald, 17489 Greifswald, Germany
[f]Maritime Systems, Interdisciplinary Faculty, University of Rostock, 18059 Rostock, Germany

[*]Corresponding author. Email address: jurjen.rooze@io-warnemuende.de (Jurjen Rooze)
[1]Current address: Organic Geochemistry Group, MARUM Center for Marine Environmental Sciences, University of Bremen, 28359 Bremen, Germany
[2]Current address: Environmental Geology Group, Institute for Geosciences, University of Bonn, 53115 Bonn, Germany.

Abstract

Trawl-fishing is broadly considered to be one of the most destructive anthropogenic activities toward benthic ecosystems. In this study, we examine the effects of bottom-contact fishing by otter trawls on the geochemistry and macrofauna in sandy silt sediment in an area of the Baltic Sea where clear spatial patterns in trawling activity were previously identified by acoustic mapping. We calibrated an early diagenetic model to biogeochemical data from various coring locations. Fitting measured mercury profiles allowed for the determination of the sediment mixing and burial

velocity. For all sites, independent of the trawl mark density, good fits were obtained by applying the model with the same organic matter loading and parameter values, while iron fluxes scaled linearly with the burial velocity. A sensitivity analysis revealed that the fitted sulfate reduction rate, solid sulfur contents, ammonium concentration, and both the isotopic composition and concentration of dissolved inorganic carbon provided reliable constraints for the total mineralization rate, which exhibited a narrow range of variability (around ±20% from the mean) across the sites. Also, the trawling intensity did not significantly correlate with total organic carbon contents in surficial sediment, indicating limited loss of organic matter due to trawling. The fits to the reactive iron, acid volatile sulfur, chromium(II) reducible sulfur contents, and porewater composition demonstrate that sediment burial and mixing primarily determine the redox stratification. The mixing depth did not correlate with trawling intensity and is more likely the result of bioturbation, as the analyzed macrofaunal taxonomy and density showed a high potential for sediment reworking. The extraordinarily long-lived *Arctica islandica* bivalve dominated the infaunal biomass, despite the expectation that trawling leads to the succession from longer-lived to shorter-lived and bigger to smaller macrofauna. Our results further suggest that a clear geochemical footprint of bottom-trawling may not develop in sediments actively reworked by tenacious macrofauna.

1. Introduction

Coastal sediments play a critical role in global biogeochemical cycles by processing high loads of organic matter (OM) and removing and recycling nutrients in ecosystems. About 70-90% of the global ocean OM burial and more than half of sedimentary OM mineralization has been estimated

to take place in continental shelf sediments that only account for 7% of the total seafloor (Berner, 1982; Middelburg et al., 1997; Thullner et al., 2009). The shelves have increasingly become exposed to bottom-trawling, affecting currently 14% of the global and >50% of the European shelf and continental slope sediments at <1000 m water depth, respectively (Amoroso et al., 2018). Currently, the consequences of this disturbance for OM storage and mineralization are not well understood and fiercely debated (Luisetti et al., 2019; Paradis et al., 2021; Sala et al., 2021; Epstein et al., 2022; Hiddink et al., 2023; Atwood et al., 2023).

The drag force exerted by trawling gears can scrape off, resuspend, and mix sediments (e.g., Palanques et al., 2001; O'Neill and Summerbell, 2011; Oberle et al., 2016). Sediment resuspension may lead to sediment coarsening and loss of organic carbon associated with fine-grained materials (Pusceddu et al., 2014; Paradis et al., 2019). Both sediment mixing and resuspension can increase OM exposure to O_2, which enhances mineralization. These impacts may be offset by the tendency of bottom-trawling to kill particularly larger animals (Kaiser et al., 2006), which decreases bioturbation (e.g., Queirós et al., 2006; Olsgard et al., 2008; McLaverty et al., 2020), i.e., the natural stirring and oxygenation of sediment by benthic macrofauna that may also enhance sediment resuspension (Hir et al., 2007). Trawling and natural disturbances can affect mineralization rates through other mechanisms: for instance, by bringing deeper buried OM closer to the sediment-water interface (SWI, Pusceddu et al., 2005), changing the benthic trophic state (Watling et al., 2001; Polymenakou et al., 2005), and by priming microbial communities at depth with fresh OM (see for more hypotheses van de Velde et al. [2018]).

Unraveling the footprint of trawling through observational and experimental studies has proven to be a daunting task. Observational studies commonly analyze statistical trends along

trawling intensity gradients (Nielsen et al., 2023). While advantageous for making inferences about long-term ecosystem impacts, these studies often rely on less reliable indices for trawling activity based on tracking data of fishing vessels (Muench et al., 2018). Furthermore, fishing activity may correlate with other environmental parameters, such as water depth and sediment substrate (Hintzen et al., 2020; Mazor et al., 2020; Downie et al., 2021; Bastardie et al., 2021), making it challenging to isolate the effects of trawling on diagenetic processes. Trawling experiments that monitor the conditions before, during, and after a trawling event or compare the effects to a control area may be better posited to uncover causal relationships. The drawback of these studies is their focus on analyzing the local effects of fresh trawl marks. Experiments typically last for one or a couple of days, limiting the quantification to short-term impacts. However, a few studies have also examined the effects of repeated trawling over several months (Lindeboom and De Groot, 1998; Smith et al., 2000; Bhagirathan et al., 2008; Ferguson et al., 2020).

A meta-analysis by Epstein et al. (2022) found that 49 studies determined the effects of bottom-trawling on carbon stocks, with 10% reporting an increase, 29% a decrease, and 61% no significant change. Only 7 studies reported the effect on benthic OM mineralization, of which 4 reported an increase and 3 a decrease in mineralization rates. Similarly, varying results have been reported concerning the effects on sediment-water exchange fluxes of nutrients and oxygen (e.g., Warnken et al., 2003; Durrieu de Madron et al., 2005; Zacharia et al., 2006; Morys et al., 2021; Bradshaw et al., 2021). Many factors may have contributed to the varying results: The fishing gear, towing intensity, and sediment lithology determine the generated drag force and amount of resuspended materials (O'Neill and Ivanović, 2016; Eigaard et al., 2015). The sensitivity of the benthic macrofauna to trawling depends on the trawling gear and characteristics of the species (e.g.,

typical life cycle, proximity to the seafloor, and body structure; Kaiser et al., 2006). At locations accustomed to sediment mixing and resuspension caused by waves and bioturbation, trawling may have less impact on the early diagenetic processes (Kaiser, 1998; Duplisea et al., 2001; Tiano et al., 2022). Long-term carbon storage requires sufficiently high deposition and mild hydrodynamic conditions for net sedimentation (Epstein et al., 2022). Other than that, benthic mineralization rates and OM burial strongly depend on the organic matter reactivity and loading, bioturbation, sedimentation rate, and type of sediment substrate, which are factors generally important for early diagenesis (e.g., Berner, 1980; Boudreau, 1997; Arndt et al., 2013).

Modeling plays a vital role in assessing the importance of anthropogenic pressures and environmental parameters, allowing for the generalization of observational and experimental findings. The impact of various trawling gear and sediment substrate on the benthic trophic state, infauna, and carbon and nutrients fluxes has been investigated in models that divide the sediment into two or three compartments, representing different redox conditions (Duplisea et al., 2001; Allen and Clarke, 2007). Recent studies have taken a step further by incorporating trawling activity in depth-resolved early diagenetic models (de Borger et al., 2021; van de Velde et al., 2018). Trawling is treated as intermittent disturbance events, whereby the mechanical impact of trawling is assumed to mix the sediment and porewater and to resuspend sediment, causing OM loss. Additionally, trawling is simulated as a factor that kills benthic macrofauna, resulting in a sudden decrease in bioturbation activity, which may recover slowly afterward (de Borger et al., 2021). Early diagenetic models allow for rates of complex processes, such as mineralization, which cannot be directly measured, to be constrained by integrating various (bio-)geochemical data. Estimates of the global impact of trawling on the carbon cycle have been modeled, relying on parameters

constrained by the models, such as OM reactivity (Sala et al., 2021; Hiddink et al., 2023; Atwood et al., 2023). However, a lack of studies integrating field data from trawled locations hinders comprehensive understanding.

In this study, we analyze biogeochemical and macrofaunal data from sediment cores obtained from locations with sandy silt sediment, experiencing varying degrees of trawling intensity (Schönke et al., 2022). The dataset is used to calibrate a model, enabling us to investigate the influence on diagenetic processes. This comprehensive approach allows for comparisons of mineralization, burial, and mixing dynamics among the locations, facilitating an assessment of the effects of both bottom-trawling and bioturbation on sediment processes.

2. Material and methods

2.1. Study site, seafloor mapping, and coring locations

The research cruise EMB238 was undertaken in May/June 2020 in the Fehmarn Belt area of the southern Baltic Sea. The aims were to survey the pre-closure conditions in a designated part of a marine protected area (MPA) and a nearby control area, where fishery will continue after the exclusion. The focus areas surveyed within and outside MPA cover 4.7 km^2 and 3.7 km^2, respectively, and lie 1.7 km apart from each other (Fig. 1). They are located west of an abrasion platform and characterized by sandy silt sediment with a fine sand component (BSH, 2016; Schönke et al., 2022), inhabited by so-called “Arctica community” (FEMA, 2013). There was a ban on targeted cod fisheries in the Baltic Sea in 2019 (ICES, 2021b,a) due to its stock collapse, but bottom-trawl fishing targeting other fish species (sprat, flatfish) remained in the MPA and also in the control area. Four sampling stations were selected in each focal area with different trawling

intensities based on an initial evaluation of preceding acoustic mapping with side-scan sonar. In 2020, technical issues with the multibeam echosounder (MBES) caused a significant data loss from outer beams. Resolving the issue resulted in better data quality and coverage in the EMB267 cruise to the same area in June 2021. However, the trawling index based on the computed volume of trawl mark incisions per 10 m x 10 m tile, using a threshold of 5 cm depth, could be calculated for both years. In this study, we adopt trawling indices based on the total furrow volume per area, as previously reported by Schönke et al. (2022) for the EMB267 cruise.

A comparison of the trawl mark patterns from the two different years showed that while the large-scale pattern across the survey area remained stable, the individual furrows showed significant local spatial variability (Schönke et al., 2022). When examining the trawl mark patterns based on MBES data in the research areas, clear trends in the trawling activity can be observed (Fig. 1). Intensive trawling occurs in the southern region of the control area, which borders an elevated abrasion platform with boulders. The high density of trawl marks running parallel to the platform (Fig. 1C) suggests that fishers expect higher catches in this area. Fishers appear to avoid a buoy northeast of the control area (Fig. 1C) and revolve around a shipwreck in the area's northwestern part within the designated MPA area (Fig. 1B). We consider 10 m x 10 m tiles with a furrow volume of more than 1 m^3 to form the main trawling lane.

2.2. Sampling devices and procedures

Sediment samples were collected using a multicorer equipped with 60 cm long acrylic tubes having a 10 cm internal diameter. Up to three parallel short sediment cores were obtained at each location, serving for both geochemical and macrofaunal analyses. Special care was taken to discard sediment cores potentially disturbed during sample collection, indicated by an inclined SWI or broken

161 characteristic structures compared to the parallel cores. Three replicate samples were collected by
162 the Van Veen grab at every location (sampling area 0.1 m^2) for sampling benthic macrofauna. At
163 each location, a surface sediment sample was taken from a separate core for later grain size (optical)
164 analyzes, whereas values for near-bottom salinity, temperature, and oxygen content were obtained
165 from CTD.

166 An underwater positioning device (EvoLogics Sinaps USBL) attached to the multicore
167 system provided a positioning accuracy of less than 1 m. Examination of sample positions overlain
168 with the acoustic map suggests that none were located directly on a trawl furrow or mound.
169 Additional information about the locations with GPS coordinates and local furrow volume is shown
170 in Table S1 in the supplement.

171 *2.3. Geochemical analyses*

172 Porewaters were collected from intact multicorer cores with rhizons (0.15 µm pore width,
173 Rhizosphere) after siphoning the overlaying water to ca. 1 cm from the SWI. Porewaters were
174 collected at 1 cm intervals from 0-5 cm depth, then from 2 cm intervals from 5-15cm depth,
175 followed by 5 cm intervals from 15-25. Immediately upon sampling, solutions were aliquoted into
176 different vials preserved for the respective analyses. Samples for DIC and $\delta^{13}C$-DIC were preserved
177 with saturated $HgCl_2$ solution and kept in exetainers dark and cool until further analysis by
178 continuous flow isotope-ratio-monitoring mass spectrometry (Winde et al., 2014). The DIC
179 concentrations and isotopic compositions were measured using a Thermo Gasbench II connected
180 to a Thermo Finnigan MAT 253 gas mass spectrometer via a Thermo Conflo IV split interface
181 (Winde et al., 2014). Samples for NH_4 were kept frozen until photometric analysis on a QuAAtro
182 multi-analyzer system (Seal Analytical, Southampton, UK; Lipka et al., 2018). Samples for

183 dissolved major and trace elements (Na, K, Ca, Mg, Li, Sr, Mn, Si, S, Fe, P) were preserved with
184 concentrated HNO_3 and refrigerated until analysis by ICP-OES (Thermo ICAP 7400; Von Ahn et
185 al., 2021). Samples for sulfide were preserved with 5% $Zn(OAc)_2$ solution and analyzed
186 photometrically (Specord 40 spectrophotometer, Analytik Jena) following the method proposed by
187 Cline (1969).

188 Sediment samples were collected immediately from intact sediment cores via extrusion at
189 1 cm intervals for the top 5 cm and 2 cm intervals for the remainder of the core. Care was taken to
190 prevent sampling of the potentially disturbed outer rim. Sediment samples were split, whereby half
191 of these were preserved with $Zn(OAc)_2$ solution and kept frozen until analysis for chromium(II)
192 reducible sulfur (CRS, mostly pyrite) and acid-volatile sulfur (AVS) via a two-step distillation
193 following Fossing and Jørgensen (1989). Sulfide concentrations were measured photometrically
194 (see above). The second half of the sediment samples were kept frozen in closed plastic vials until
195 subsequent analysis of water content via mass loss upon freeze drying, from which the porosity
196 was calculated. The freeze-dried sediment was homogenized and analyzed for total carbon, total
197 nitrogen, and total sulfur (TC, TN, TS) with a Eurovector elemental analyzer, total inorganic carbon
198 (TIC) with an Analytik Jena analyzer using infrared spectroscopy after phosphoric acid reaction
199 and total mercury (THg) with a DMA 80 element analyzer (Leipe et al., 2013). The total organic
200 carbon (TOC) content was calculated from the difference between TC and TIC (Al-Raei et al.,
201 2009). Freeze-dried sediments were extracted with 0.5 M HCl to obtain extractable major, minor,
202 and trace metal contents (Ca*, Mg*, Sr*, Fe*, Mn*, Pb*, Cd*, Zn*) and phosphorus (P*) that were
203 analyzed by ICP-OES (Thermo iCAP 7400; e.g., Von Ahn et al., 2021).

2.4. Sulfate reduction rate measurements

Sulfate reduction rates (SRR) were quantified using incubations of intact sediment cores with radioactive $^{35}SO_4^{2-}$ radiotracer (Jørgensen, 1978). Using a single multicorer core per sampling site, three 40 cm-long acrylic tubes (30 mm OD, 24 mm ID) were pushed vertically into the sediment to retrieve mechanically undisturbed subcores. Along its side, each tube has a single row of 2 mm holes drilled in 1 cm resolution, the holes are sealed with silicone to avoid seepage of porewater but allow injection of radiotracer. When inserting the acrylic tubes, suction was applied to avoid compression of the sediment. The subcores always contained more than 20 cm of sediment and a few of the overlying bottom water to allow for undisturbed incubations from the SWI down to 20 cm. Immediately after retrieval of the multicorer, the core was subsampled and the three subsampling tubes stored in an incubator at approximately in-situ temperature (10 °C). Incubations were initated the same day. For incubation, 200 kBq of radiotracer was injected into each hole from the SWI down to 20 cm. Immediately after injection of radiotracer, the core tube was put back into the incubator and incubated for 24 h. Incubations were terminated by pushing the sediment out of the subsampling tubes, slicing them into depth sections and transferring the sediment into 50 mL centrifuge tubes, filled with 10 mL of 20% (w/v) zinc acetate solution. Before slicing, the remaining bottom water was siphoned off with a syringe and treated the same way as sediment samples. The following depth resolution was used on all cores: 0-6 cm: 1 cm, 6-10 cm: 2 cm, 10-20 cm: 5 cm. The vials were thoroughly shaken to break up all sedimentary structures and effectively stop all microbial activity. Due to lack of freezer space the fixed samples were stored at room temperature. Back in the home lab, the microbially produced reduced inorganic sulfur compounds (TRIS, total reduced inorganic sulfur) were separated from the bulk sample using cold chromium distillation

(Kallmeyer et al., 2004). Radioactivity was quantified by scintillation counting.

2.5. Macrofaunal analysis

Sediment from grab samples included in this study was sieved using a 1.0 mm sieve mesh size. Ten sediment cores were also sliced (in 2 cm steps down to 10 cm sediment depth, 10-15 cm, and the rest below 15 cm) and sieved using a 0.5 mm sieve mesh size to estimate the vertical distribution of macrobenthos. Biological material was preserved in a 4% buffered formaldehyde–seawater solution. In the laboratory, the organisms were sorted, identified to species level (with the exception of genus *Phoronis* and family *Naididae*), and counted and weighted to obtain data on species abundance and biomass. The nomenclature followed the World Register of Marine Species (WoRMS Editorial Board, 2020).

The bioturbation potential (BP_c; Solan et al., 2004) was calculated for each sample as a proxy for sediment mixing activity, following the methodological details described in Gogina et al. (2020). It is defined as

$$BP_c = \sum_{i=1}^{n} \sqrt{\frac{B_i}{A_i}} A_i M_i R_i$$

where, for each taxon (i), B_i/A_i is the mean individual biomass, and A_i is the abundance (units individuals/m^2) at each sample. M_i and R_i are categorical scores for mobility and sediment reworking, respectively, assigned to each taxon based on ecological knowledge. In cases where trait categories were deemed irrelevant or negligible concerning sediment mixing or solute exchange across the sediment-water interface (e.g., for epifauna), a score of zero was assigned, leading to no contribution of specific species to BP_c.

2.6. Description of the early diagenetic model

A reaction-transport model was applied, simulating the key dynamics of coupled benthic oxygen, nitrogen, manganese, iron, sulfur, and carbon cycles during early diagenesis. It follows a classical approach (Wang and Van Cappellen, 1996; Boudreau, 1997) without accounting explicitly for bottom-trawling events.

2.6.1. Transport and governing equations

The concentration profiles of solids and solutes were described as

$$(1-\phi)\frac{\partial C_i}{\partial t} = \frac{\partial}{\partial z}\left[(1-\phi)D_T\frac{\partial C_i}{\partial z} - (1-\phi_\infty)w_\infty C_i\right] + \sum_k (1-\phi)\,\gamma_{i,k}R_k \quad (1)$$

and

$$\phi\frac{\partial C_j}{\partial t} = \frac{\partial}{\partial z}\left[\phi(D_m\theta^{-2} + D_T)\frac{\partial C_j}{\partial z} - \phi_\infty w_\infty C_j\right] + \sum_k \phi\,\gamma_{j,k}R_k + \phi\alpha(C_0 - C_j) \quad (2)$$

respectively, whereby ϕ is the fitted porosity, w is the burial velocity, R is the reaction term, γ denotes the stoichiometric coefficient for reactions, D_m is the molecular diffusivity, θ^2 is the sediment tortuosity, D_T is the turbation diffusivity, and α is a non-local transport parameter (Boudreau, 1997). The molecular diffusivities were corrected for salinity, temperature, and pressure, which were set to 18.8, 10 °C, and 2 bar, respectively. For DIC and alkalinity the diffusivity of HCO_3^- was used. Subscripts 0 and ∞ indicate evaluation at the SWI and below the compaction zone, respectively, throughout the text. The terms containing D_T and α commonly represent bioturbation in the form of biodiffusion and bio-irrigation, respectively (Boudreau, 1997; Kristensen 190 et al., 2012), but here we will refer to it as turbation and non-local transport, as it may also account for disturbances caused by bottom-trawling. The vertical profiles of the fitted

porosity (ϕ), turbation (D_T), and non-local transport (α) each follow an exponential decay function

$$\psi^E = \psi_0^E - (\psi_0^E - \psi_\infty^E)e^{-z/\eta^E} \quad (3)$$

whereby uppercase 'E' is replaced by the respective symbols to distinguish the profiles of different parameters, ψ_0^E is the fitted value at the SWI, and η^E is the fitted e-folding distance. $\psi_\infty^{D_T}$ for turbation ($E = D_T$) is set to 0. In the baseline simulations, irrigation ($E = \alpha$) is turned off, and in separate testing simulations where it is turned on, it decays to 0 at depth (i.e., $\psi_\infty^\alpha = 0$). For porosity ($E = \phi$), ψ_∞^ϕ is the porosity below the compaction zone. For unit conversions, a solid-phase density of 2.6 g cm^{-3} was assumed.

2.6.2. Constraining solid-phase transport by fitting measured mercury profiles

To constrain the transport of solids, we first fitted mercury (Hg) profiles in a separate model. Mercury is a contaminant released in large quantities in the Baltic Sea from the 1950s until the 1970s/1980s, after which the inputs decreased (Leipe et al., 2013). The imposed flux for metals at the SWI is modeled as

$$F^M = \zeta_0^M + (1 - \phi_\infty)w_\infty\zeta_1^M \quad (4)$$

For mercury (M = Hg), the parameter ζ_0^{Hg} was set to 0, and ζ_1^{Hg} was fitted as a time-dependent parameter (see the results section). At the bottom, a zero-gradient boundary condition was imposed. The model did not account for reactions. We have tested the effect of desorption in a model (not shown) but found that it had a negligible effect on the solid-phase Hg content, as Hg adsorption to sediment is strong ($K \approx 10^{3.3}$ kg/L; Hollweg et al., 2009). The ReacTran package in R (Soetaert and Meysman, 2012; R Core Team, 2022) was used to implement Eq. 1, whereby a model domain length of 30 cm was discretized by 150 evenly spaced cells. Starting from initial concentration set

to zero, the model was run to a steady state.

2.6.3. Constraining solid-phase transport by fitting measured mercury profiles

Reactive particulate organic matter (POM) is represented by a single state variable, and unreactive POM is not explicitly modeled. Table 1 shows an overview of all the state variables used in the model. The model tracks the isotopic composition of dissolved and solid carbonates. Both iron and manganese oxide are represented by two state variables (i.e., MnO_2^{α}, MnO_2^{β}, $Fe(OH)_3^{\alpha}$, $Fe(OH)_3^{\beta}$, of which only the α-fractions react with organic matter. This can represent the effect of different crystallinities, allowing metal oxides to reach deeper sediment layers (Wang and Cappellen, 1996; Berg et al., 2003). Assuming dissolved acid-base chemistry to be in equilibrium, the pH was computationally derived from total alkalinity (TA), dissolved inorganic carbon (DIC), total dissolved sulfide, total reduced nitrogen, and a constant value representative of the overlying water for the total borate ion concentration (Hofmann et al., 2010).

The model includes all major mineralization pathways (R_1 to R_5, Table 2) except methanogenesis, which is assumed to be inhibited by the presence of SO_4^{2-}. Oxygen can reoxidize reduced metabolites (R_6 to R_9) and react with the minerals FeS, FeS_2, and S_0 (R_{10}, R_{15}, R_{17}, respectively). MnO_2 can reoxidize H_2S, Fe^{2+}, and S_0 (R_{12}, R_{13}, R_{18}, respectively), while $Fe(OH)_3$ only reoxidizes sulfide (R_{11}). FeS_2 formation can occur through a reaction between the intermediates FeS and S_0, and also between FeS and H_2S (Rickard and Luther, 2007), whereby the produced H_2 is assumed to react immediately with SO_4^{2-} (R_{16}). Reactions R_{19} and R_{20} account for MnO_2 and $Fe(OH)_3$ crystallization, respectively. R_{21} and R_{22} account for the precipitation and

dissolution of $CaCO_3$ and FeS, respectively.

The kinetic rate laws and rate constants for all reactions are shown in Table 3. Aerobic respiration is assumed to be 100 times kinetically faster than the anaerobic pathways (Table 3). Mineralization of POM releases DIC with an isotopic composition −22‰ (all reported $\delta^{13}C$ values are relative to the V-PDB standard), which is considerably lighter than DIC and TIC from the overlying water ($\delta^{13}C$ = −2‰, Table 4). Isotope fractionation factors for the reaction pathways considered in the model are small and ignored (Meister et al., 2019). A high value for the rate constant of Fe^{2+} oxidation limited the escape of Fe^{2+} to the overlying water (k_8, Table 3), which typically should be less than 5 mmol m^{-2} y^{-1} in settings without bio-irrigation (Raiswell and Canfield, 2012).

For the solids, fluxes were imposed as upper boundary conditions (Table 4). The fluxes of MnO_2 and $Fe(OH)_3$ depended linearly on the sediment accumulation rate, as described by Eq. 4 (see ζ_0^M and ζ_1^M in Table 4). Fixed concentrations representative of bottom water were imposed as upper boundary conditions for solutes (Table 4). The zero-gradient condition prescribed the lower boundary condition for all state variables. To establish initial conditions across the domain, the concentration of TIC was initialized to a small value (1%) with $\delta^{13}C$ = −2‰, while the DIC and Ca^{2+} were prescribed with representative values of the overlying water (Table 4). The alkalinity was adjusted to 1.2 times the value found in the overlying water to ensure oversaturation with respect to TIC. All other state variables were set to zero.

The domain covering the distance from the SWI to a depth of 61 cm was discretized in an uneven grid with 40 cells and cell distances ranging from 1 mm at the top to 2 cm at depth. Applying the modeling framework developed by Rooze et al. (2020) and Zindorf et al. (2021) for R (R Core

Team, 2022), reaction rates resolved by CVODE (Hindmarsh et al., 2005) were coupled with transport following the sequential iterative operator splitting approach (Steefel and MacQuarrie, 1996). The simulations were run to a steady state.

2.7. Data integration

2.7.1. Modeling approach

The integrated organic matter mineralization rate in the model at steady-state equals the reactive organic matter input F_{POM}. The most effective parameters for constraining mineralization in the model are the sulfate reduction rates, the DIC and NH_4^+ concentrations produced during mineralization, and the in-situ $\delta^{13}C$-DIC resulting from the distinct isotopic signatures of −2‰ and −22‰ of inorganic carbon from the overlying water and POM, respectively. Redox stratification, strongly impacting the sulfur-metal dynamics, was constrained by the degree of pyritization (DOP), the penetration depth of reactive iron oxides, the ferruginous-sulfidic transition depth, and the SRR profiles.

2.7.2. Data and model comparison

The measured TOC is interpreted as particulate organic carbon (POC), which is related to particulate organic nitrogen and phosphorus through the adapted Redfield ratio (C:N:P = 122:16:1). Only POM that is reactive in the upper sediment is explicitly modeled. In plots of simulated reactive POM, the average measured TOC concentration below 15 cm is added and considered a refractory fraction, which allows a better comparison between modeled and measured TOC. Similarly, the

model only includes reactive solid metals and the unreactive fraction is removed from the plots. To compare the iron extraction results to the model results, the measurements are interpreted as

$$[Fe(OH)_3] = Fe^* - Fe_{AVS} - Fe_U^* \quad (5a)$$

$$[FeS] = Fe_{AVS} \quad (5b)$$

$$[FeS_2] = Fe_{CRS} \quad (5c)$$

$$DOP = [FeS_2] / ([Fe(OH)_3] + [FeS] + [FeS_2]) \quad (5d)$$

whereby Fe_U^* is the mean Fe* concentration below 15 cm depth, which is considered to be refractory. Fe_{CRS} can also include extracted S_0, which is here ignored, as in the model the amount of S_0 compared to FeS_2 was negligible. DOP is an abbreviation for degree of pyritization. The measured Mn* is interpreted as MnO_2, ignoring possible contributions of other manganese minerals.

Relative errors reported in the text are only determined in the upper 10 cm of sediment and defined for single profiles as

$$\epsilon = \frac{\sum_{i=1}^{n}(\hat{y}_i - y_i)^2}{n\bar{y}^2} \quad (6)$$

whereby y_i and $\hat{y}_i$ are the measurement and model interpolated value at the same depth, n is the number of measurements, and $\bar{y}$ is the average measured value. The overall error of multiple fits was quantified by averaging the errors of several profiles.

3. Results

3.1. Solid-phase sediment deposition and mixing

Metal profiles of extractable lead, zinc, cobalt, and copper appeared similar to total bulk Hg (THg; Spearman correlation coefficients: 0.91, 0.88, 0.84, 0.83, respectively), indicating similar depositional history and conservative behavior. TOC content was strongly correlated with porosity (Spearman's rank correlation: r[128]=.82) and to a lesser extent with THg (r[127]=.50; shown for site 2 in Fig. 2A,B,C).

Fitting the mercury profiles resulted in an approach whereby the Hg content in deposited sediment was set to 13 µg g^{-1} before 1950, 150 µg g^{-1} from 1950 to 1980, and a linear decrease from 150 µg g^{-1} to 30 µg g^{-1} between 1950 and 2020 (ζ_1 in Eq. 4; Fig. 2F). By imposing this pattern for all sites, the sediment accumulation rate w_∞ and the turbation e-folding distance η_T^D (Eq. 3; Table 5) were fitted to the measured THg profiles (Fig. 2C,D,E) for each individual site. In this approach, w_∞ determines the total Hg input, and turbation affects the shape of the Hg profile.

Sites 10, 13, and 18 had slower solid-phase transport, as lower w_∞ and η_T^D values indicated (w_∞: 0.2 – 0.4 mm y^{-1}; η_T^D: 0.6 – 1.2 cm; Table 5). Conversely, solid-phase transport was faster at sites 2, 5, 8, 15, and 17 (w_∞: 0.4 – 1.2mm y^{-1}; η_T^D: 1.3 – 2.2 cm; Table 5). The fitted Hg profiles for sites 10, 13, and 18 with slower transport are shown in Figure 3, and for sites 2, 8, and 15 with faster transport in Figure 4. See supplementary Figure S1 for the profiles of sites 5 and 17.

3.2. Trends in (bio-)geochemical profiles: Comparison of model results to measurements

The biogeochemical data and model fits are shown in separate figures for sites with slower (Fig. 3) and faster solid-phase transport (Figs. 4 and S1). The distributions of the modeled mineralization rates over depth exhibit sensitivity to solid-phase transport, with more mineralization occurring near the SWI in cases of slower transport compared to faster transport (compare SRR profiles in Figs. 3 and 4). In the model, faster burial and deeper mixing of solids lead to higher NH_4^+, PO_4^{3-}, and DIC accumulation and more negative $\delta^{13}C$ values at depth (Figs. 3, 4, S1). The sites with slower solid-phase transport (10, 13, 18) show $Fe(OH)_3$ and MnO_2 reaching less deep into the sediment (modeled $Fe(OH)_3$ reaches 5 – 7 cm depth, Fig. 3) and a steeper slope of the DOP profile (Fig. 3). Conversely, Fe* and Mn* reach deeper and the DOP profiles exhibit a lower slope at sites 2, 5, 8, 15, and 17 with faster solid transport (modeled $Fe(OH)_3$ reaches 7.5 – 9 cm depth, Figs. 4, S1). The model generally fits the measured $Fe(OH)_3$, FeS_2, and DOP slope at various sites well. The measured solid P profiles closely follow the measured Fe* trends, which is simulated by a fixed P:Fe adsorption ratio in the model (Figs. 3, 4, S1).

The measured SO_4^{2-} and Ca^{2+} concentrations tended to increase over depth following a trend of increasing salinity. In Figures 3, 4, and S1, the trends are removed by scaling the measured concentrations to salinity and compared to SO_4^{2-} and Ca^{2+} profiles produced by the model, which did not account for changes in salinity. The magnitude of maximum Fe^{2+} and H_2S concentrations can differ strongly between core duplicates (compare different symbols representing measurements from duplicate sediment cores in Figs. 3 and 4) and can show large deviations from the modeled values. Generally, H_2S accumulation at depth is underestimated by the model. The measured Ca^{2+}

409 concentrations corrected for salinity match well with the simulations and indicate conservative
410 behavior (Figs. 3 and 4). The measured TIC concentrations often show a decrease at depth at the
411 sites with faster transport (Figs. 3, S1), which the model did not reproduce.

412 Fitting the biogeochemical datasets converged in an approach whereby the POM
413 degradation rate parameter (k, Table 3) and the POM loading (F_{POM}; Table 4) and, hence, the depth-
414 integrated mineralization rates are the same at all sites. Also, the same rate constants for other
415 reaction pathways were kept constant (Table 3). The effect of changing the reactive POM loading
416 is shown in Fig. 5. For all sites, increasing or decreasing the fluxes by 20% worsened the fits of
417 profiles considered to be directly related to mineralization (sect. 4.1.1), except for sites 5 and 8,
418 where lowering the POM loading improved the fits slightly.

419 The reactive POM included in the model constitutes only a relatively small fraction of the
420 total measured TOC concentrations (Figs. 3, 4, S1). Considering the effects of environmental
421 parameters on carbon storage, the data indicate that the TOC contents in the upper 5 cm layer did
422 not correlate significantly with trawling intensity ($r = .14$, $p = .783$), sediment accumulation rate
423 ($r = -.19$, $p = .665$), turbation mixing depth ($r = .10$, $p = .840$), or water depth ($r = .08$, $p =$
424 $.845$).

425 ### *3.3. Macrofaunal analysis and bioturbation potentials*

426 Overall, a total of 87 macrofauna taxa were recorded in samples. The biomass comprised up to
427 93% of *Arctica islandica*, an active suspension-feeding long-lived bivalve, scored as a surficial
428 modifier and classified as critically endangered ((HELCOM Red List Biotope Expert Group, 2019).
429 Results support the presence of the typical *Arctica* community in the aphotic fine-grained sediment

at all locations independent of trawling intensity. The contributions to total abundance were more evenly distributed between different taxa (dominated by few bivalves, the brittle star *Ophiura albida*, cumacean *Diastylis rathkei* and few polychaete species, including *Scoloplos armiger* and *Nephtys ciliata*, see Table S2).

The unitless bioturbation potentials based on the macrofauna showed considerable variability, occasionally also between duplicate cores or nearby locations. For example, in one multicorer cast from site 5, BP_c ranged from 795 to 1526 across three replicate cores. At sites 10 and 13, which are approximately 70 meters apart, BP_c was estimated as 318±84 (mean±SD) and 460±12, respectively, in grab samples. Spatial patterns were explored by evaluating their correlation with the distance from the main trawling lane (DTL), the trawling indices (TI), and water depth (Fig. 6). The correlation between the community bioturbation potential and TI was stronger for larger than for smaller tiles (75 m x 75 m compared to 10 m x 10 m tiles, Fig. 6). Surprisingly, BP_c correlated strongest with water depth. Other abiotic factors such as near-bottom oxygen concentrations, salinity, granulometry parameters (not shown), and total organic content of surface sediments (Fig. 6) were also tested, but the association with them was less strong. The trawling indices and DTL also strongly correlated with water depth (Fig. 6). Calculation of the semi-partial Spearman correlation coefficients that removed the variability in water depth from TI and DTL resulted in a correlation reduction from -0.56 to -0.13 between BP_c and TI 75 m x 75 m and from 0.60 to 0.15 between BP_c and DTL. Similarly, semi-partial correlation coefficients between *A. islandica* biomass and TI 75 m x 75 m and DTL, when controlling for water depth, were -0.17 and 0.21 (comparing to -0.40 and 0.43 before detrending), respectively, and were both not significant anymore.

4. Discussion

General hypotheses considering the effects of bottom-trawling on sediment transport and OM mineralization are displayed in Figure 7 and summarized in the following: Bottom-trawling disturbs the seafloor mechanically (link 1, Fig. 7). The mechanical force exerted by trawls is expected to mix sediment (link 2), kill animals (link 3), and resuspend sediments (link 4). The killing of animals decreases bioturbation (link 5) and may also have a weak negative effect on the erodibility and resuspension of sediment (link 6). Sediment mixing may enhance benthic mineralization (link 7). Sediment resuspension leads to a loss of sedimentary OM, which decreases benthic mineralization rates (link 8, Fig. 2). The extent to which the biogeochemical data and modeling support the hypotheses and allow for the rejection of the null hypothesis of no trawling impact will be discussed in detail in sections 4.1, 4.2, and 4.3, accompanied by a summary overview provided in Figure 7. Finally, section 4.4 discusses the environmental context relevant for generalizing the findings.

4.1. Reaction-transport dynamics in relation to bottom-trawling and bioturbation in the study area

First, the interpretation of Hg profiles in relation to solid-phase transport and trawling will be discussed (sect. 4.1.1). Then the model performance and reliability concerning OM mineralization (sect. 4.1.2) and redox stratification (sect. 4.1.3) will be evaluated. Finally, the impact of trawling on the sediment biogeochemistry is discussed in section 4.1.4.

4.1.1. Interpretation of mercury profiles

Sediment resuspension decreases net sediment accumulation over time. Sites 10 and 13, located in a heavily trawled area, have slow sedimentation rates, consistent with sediment loss due to trawling. Overall, there is a negative correlation between trawling intensity and sediment accumulation rate, which is significant depending on the correlation method used (Pearson correlation: $r[5] = -.63$, $p = .128$; Spearman's rank correlation: $r[5] = -.96$, $p = .003$). Site 8 forms an exception with a high trawling index (Table S1) and fast sediment accumulation (w_∞, Table 5). The limited number of stations examined for geochemical analysis, i.e., corresponding to 5 or 6 degrees of freedom, prevent robust statistical analysis, particularly since the distance between sites with similar trawling indices is not random, and spurious correlations may result from covariations with other environmental parameters. Sites 10 and 13 are located at the shallowest depths in each other's vicinity, close to an abrasion platform (Fig. 1A,C). The bathymetry likely affects the sediment accumulation rates, despite a relatively weak correlation in the data (Spearman's rank correlation: $r[6] = .48$, $p = .230$). Hence, the effect of trawling intensity on w_∞ remains unclear (link 4, Fig. 7).

Bottom-trawling may also induce sediment mixing (link 2, Fig. 7). Of the sites with high trawling indices, sites 10, 13, and 18 exhibited shallow mixing depths, and site 8 experienced deeper mixing η^{D_T}, Table 5). There is an insignificant (negative) correlation between mixing depth (η^{D_T}, Table 5) and trawling index (Spearman's rank correlation: $r[5] = -0.57$, $p = .200$) since other sites with deeper mixing have lower or zero trawling indices (site 2, Table S1). Bioturbation could be responsible for the mixing at both more and less intensely trawled areas, as bioturbation potentials did not significantly correlate with the trawling index. Due to the very patchy distribution

of macrofauna and the distance between sampling locations for geochemical and macrofaunal analysis, the mixing depths (η^{D_T}) obtained by fitting mercury profiles cannot be directly compared to determined bioturbation potentials. However, given the insignificant or negative correlation between trawling intensity and mixing depth and the generally high bioturbation potentials, bioturbation is most likely responsible for the observed mixing (link 5, Fig. 7).

4.1.2. Validation of modeled mineralization processes

Mineralization rates imposed in the model are mostly inferred from measured SRRs, total sulfur solids, NH_4^+, DIC, and δ^{13}C-DIC. The measured SRRs provide a direct estimate of in-situ mineralization at the time of sampling. The model successfully captured a trend of a deeper sulfate reduction zone, attributed to increased sediment mixing at greater depths (Table 5, Fig. 4). The inhibition of sulfate reduction near the SWI caused by metal oxides following the diagenetic sequence (i.e., the consumption of terminal electron acceptors in order of decreasing energy yield; Froelich et al., 1979; Berner, 1980) often appeared to be overly pronounced (see sites 2, 8, 15 in Fig. 4). However, as most sulfide produced during SRR binds to iron, the well fitted FeS_2 profiles and the total accumulation of sulfur solids support the modeled depth-integrated SRRs. In addition, FeS_2 accumulation may provide a better measure for long-term average SRRs, as it is less affected by seasonality and short-term disturbances compared to aqueous-phase chemistry. The fits of DIC and NH_4^+ support the modeled mineralization rate, as higher mineralization rates would have led to higher DIC and NH_4^+ concentrations and more negative δ^{13}C-DIC values. There is some uncertainty in the DIC and NH_4^+ profiles due to the potential role of bio-irrigation. Particularly for site 5, imposing bio-irrigation ($\psi_0^\alpha = 10$ y^{-1}, $\eta^{D_T} = 3.3$ cm; Eqs. 2, 3) improved these fits but

517 worsened the fit of FeS_2 at steady-state (Fig. S1).

518 The measured TOC contents do not provide a quantitative constraint for mineralization
519 because most of the present TOC appears to be refractory on time scales for early diagenesis. With
520 depth, TOC and porosity increase and decrease simultaneously (sect. 3.1, Fig. 2A,B), indicating
521 non-steady state sediment deposition and possibly a lithological control. The TOC contents in the
522 upper 5 cm showed no significant correlation with trawling intensity or other environmental
523 parameters (sect. 3.2). The C:N ratios of TOC varied between 7.7 and 12, indicating a predominant
524 marine source of OM (Rullkötter, 2006), which tends to be more labile than terrestrial OM. The
525 relatively featureless siliciclastic grain size distributions over depth (not shown) did not follow the
526 trends in porosity, which may indicate that the biogenic contents (i.e., organics and carbonates)
527 removed for this analysis play an important role in the coating of grains and thereby providing
528 physical protection to mineralization (Keil et al., 1994; Mayer, 1994), while early compaction of
529 clay minerals may also take place (Böttcher et al., 2000; Al-Raei et al., 2009).

530 The legacy of episodic saltwater inflows from the North Sea (e.g., Naumov et al., 2023) and
531 recent freshening led to an increasing trend of porewater salinity over depth. It strongly influenced
532 ion profiles with slower turnover rates. Cations such as Ca^{2+} (Figs. 3, 4, S1) and Sr^{2+} (not shown)
533 generally followed the salinity trends (not shown), indicating limited precipitation/dissolution of
534 carbonates, despite the decline at depth in measured TIC values not reproduced by the model. One
535 of the duplicate cores of site 18 formed an exception, as a clear peak in Ca^{2+} indicated recent $CaCO_3$
536 dissolution (Fig. 3). The SO_4^{2-} concentrations also increased with salinity over depth, masking the
537 effect of sulfate reduction. The model did not account for changes in bottom-water salinity, and the
538 sulfate profiles were, therefore, not used to constrain sulfate reduction. Nevertheless, the modeled

profiles look similar to the measured values scaled to salinity (Figs. 3, 4, S1), which supports the modeled turnover rates.

4.1.3. Validation of modeled redox stratification

The DOP profiles show the conversion of $Fe(OH)_3$ to FeS_2 over depth, indicating the change in redox conditions. $Fe(OH)_3$ reaches deeper and DOP gradients are less steep at sites 2, 5, 8, 15, and 17 (Figs. 4, S1) compared to sites 10, 13, and 18 (Fig. 3). This is the result of differences in mixing, which is well-predicted by turbation diffusivity profiles (D_T, Table 5) obtained by fitting the Hg profiles. At sites with lower turbation (i.e., mixing decaying faster with depth), mineralization takes place closer to the SWI, favoring aerobic mineralization and leading to significantly lower depth-integrated SRRs (e.g., sites 10 and 13; Fig. 3). The modeled $Fe(OH)_3$ and FeS_2 generally agree well with the measurements.

Similar to $Fe(OH)_3$, the penetration depth of MnO_2 depends on the redox zonation. There is a high local spatial variability in both Fe^{2+} and Mn^{2+}, as shown by comparing profiles from duplicate cores (Figs. 3 and 4). Both benthic Mn and Fe dynamics are strongly affected by reactions with H_2S, which also varies between duplicates and is often not well reproduced by the model. Significant mismatches emerged between modeled and measured MnO_2 profiles at sites 2 and 15 (Fig. 4). Dissolved Mn^{2+} is less quickly reoxidized than Fe^{2+}, making it more mobile (Kowalski et al., 2009) and sensitive to turbation (Schaller, 2014). Therefore, Mn contents, compared to Fe, may have been less well predicted by the modeled w_∞-dependent linear relationship (Eq. 4).

4.1.4. Bottom-trawling effects on sediment mineralization rates and organic matter loss

The classical early diagenetic model, simulating vertically stratified redox zonations at steady-state, could reproduce the main features in the porewater chemistry and solid phases. Contrary to the expected disturbances caused by trawling, the DOP and sulfur solids exhibited consistent trends over depth (Figs. 3, 4, S1), similar to the uninterrupted heavy metal contamination trends observed since the 1950s. They do not point towards irregular mixing events associated with trawling events. The same labile POM flux imposed for all sites in the model (F_{POM}, Table 4) and the sensitivity analysis showing that a change of 20% in the labile POM flux generally worsened the fits (Fig. 5) clearly suggest that the available reactive POM does not scale with the sedimentation rates, varying by a factor of 7 (Table 5). In contrast, a strong correlation between mineralization rates and sediment accumulation rates would be expected to result from a loss of POM associated with resuspended sediment. Since this is not the case, bottom-trawling appears not to cause significant loss of sediment and organic matter (links 4, 8; Fig. 7).

In our model formulation, the higher kinetic rate constant applied for aerobic respiration (R_1, Table 3) allows oxygenation to lead to faster mineralization. Therefore, it does not contradict experimental studies that showed short-term differences in sediment O_2 uptake within a day after trawling (e.g., Morys et al., 2021, link 7 in Fig. 7). However, since all reactive POM is mineralized within the model domain, our results indicate that mineralization rates integrated over depth corresponding to decades of sediment deposition are not significantly affected by trawling (link 7 not supported, Fig. 7).

4.2. Reaction-transport dynamics in relation to bottom-trawling and bioturbation in the study area

Arctica islandica strongly dominated the macrofaunal biomass (Fig. 6; Table S2) and effectively determined the bioturbation potential. This clam species is a burrowing suspension feeder with short siphons. It can have an extremely long life span (up to 70-80 years in the Baltic Sea and over 200 years in the Atlantic) and becomes sexually mature after ~ 5-10 years s (Zettler et al., 2001; Thompson et al., 1980a,b). Their prevalence in the southwestern part of the Baltic Sea largely results from their ability to cope with hypoxic conditions, as they can switch to anaerobic metabolism for up to several days (Taylor, 1976). Variable salinity and depleted oxygen conditions with oxygen levels below 1 ml/l commonly occur in the study area for 20 to 40 days per year (Gogina et al., 2014; Friedland et al., 2023). Adults may survive over 8 weeks without oxygen and over 6 weeks even under euxinic conditions. Exposure to hypoxia is more severe for larvae and juveniles, who are also more exposed to predation (Vaquer-Sunyer and Duarte, 2010). As a result, favorable environmental conditions for successful recruitment and larval survival may occur sporadically only once in several years.

The slow life cycle and infrequent recruitment worsen the ability of macrofauna to recover after a mass mortality event, and suspension feeders in fine-grained sediments are more vulnerable to the mechanical effects of bottom-trawling (link 3, Fig. 7; Kaiser et al., 2006; Allen and Clarke, 2007). It is, therefore, unsurprising that *A. islandica* is considered to have low resistance and resilience and high sensitivity to bottom-trawling (Tyler-Walters and Sabatini, 2017). The otter boards used for trawling in the Baltic Sea have been shown to damage shells of *A. islandica*, making it more vulnerable to predation (Rumohr and Krost, 1991; von Arntz and Weber, 1970). During

sampling, we also observed broken and empty shells. Unfortunately, there is no good baseline for comparison to estimate the isolated impacts of trawling, as gradients in salinity, oxygen levels, and bathymetry lead to large spatial variability of macrofauna in the Baltic Sea. It is unclear to what extent the communities are adapted to motorized bottom-trawling activities taking place since the 1930s (Schacht and Voss, 2022).

The negative correlation between bioturbation potential and water depth (which varies only in a very limited range; see Fig. 6) suggests the significant cumulative effect of this complex factor. Even at such a fine spatial scale, it integrates the effects of several other factors, including bottom currents, supply of fresh organic matter for suspension feeding, and hydrodynamics of particles resuspended by trawling. The routes of trawlers may also follow convenient isobaths and alignments or sediment types to some extent reflected by bathymetry. Correlations between macrofaunal variables and trawling index were stronger in larger tiles (compare 75 m x 75 m to 10 m x 10 m, Fig. 6), suggesting that the trends are not driven by recent trawling activity. Smaller tiles provide more precise estimates of the present furrow volumes in the near environments of coring locations; conversely, larger tiles may provide more robust estimates of average trawling activity on longer decadal time scales. Bioturbation potential, driven mainly by *A. islandica* ($r = 0.87$), also shows the strongest negative association with water depth, followed by the distance to the main trawling lane derived from aggregated data. Remarkably, as the correlations between both BP_c and trawling intensity and BP_c and distance from the main trawling lane become insignificant when detrended for water depth (see Results, sect. 3.3), the data does not provide any solid evidence for an adverse effect of trawling on bioturbation in our study area (link 3 not supported, Fig. 7).

4.3. Theoretical considerations: assessing trawling's influence on sediment turbation and resuspension, and estimating trawling frequency

Bottom-trawling is considered to disturb the sediment directly by inducing mixing and sediment resuspension. Yet, our analysis did not identify clear traces from either process or their impact on OM mineralization. Here, we interpret these observations with estimations of physical transport caused by trawling in the context of previous modeling studies (sect. 4.3.1 and 4.3.2) and consider the chance that a random sampling location has been trawled in the past (sect. 4.3.1 and 4.3.2).

4.3.1. Sediment mixing in trawled and bioturbated sediment

In previous model studies, bottom-trawling was simulated to cause intermittent mixing of solids and porewater (link 2 in Fig. 7; de Borger et al., 2021; van de Velde et al., 2018). Discrete and continuous mixing models are mathematically closely related and may produce indistinguishable chemical profiles (Meysman et al., 2003; Boudreau, 2005). Intermittent mixing in the upper sediment can be mimicked by continuous diffusion with a diffusivity of $D = 0.5f(L/3)^2$, whereby f is the trawling frequency, L is the depth of the mixed layer, and $L/3$ is the statistically average vertical distance over which a particle is moved during a single mixing event. When values for trawling frequency (e.g., 6 y^{-1}) and depth (5 cm) are inserted, diffusivity coefficients on the order of 10 cm^2 y^{-1} are obtained, which lies within the range of literature values for biodiffusion coefficients (Middelburg et al., 1997). Mixing of porewater caused by trawling has been simulated by imposing a linear concentration profile between the bottom-water concentration and the in-situ concentration at depth L before trawling (de Borger et al., 2021). In a time-continuous formulation,

this may be better represented by a non-local exchange term (see the last term in Eq. 2) than diffusion to allow more reactive chemicals, such as oxygen, to penetrate deeper into the sediment. As an end-member case for a highly reactive chemical, the expression of $\alpha \equiv f(1 - z/L)$ can be derived, whereby both the maximum irrigation intensity ($\alpha[z = 0]$) and irrigation depth (L) are low compared to typical values used for simulating bio-irrigation (e.g., Meile and Cappellen, 2003). Hence, bioturbation may be indistinguishable from or exceed mixing caused directly by trawling (links 2, 5; Fig. 7).

4.3.2. Estimating effects of bottom-trawling-induced sediment resuspension

Sediment resuspension caused by bottom trawling can impact biogeochemistry by shifting mineralization from sediment to the overlying water (van de Velde et al., 2018). De Borger et al. (2021) modeled that each trawling event eroded an upper layer with a thickness ranging from 3 to 15 mm, while Allen and Clarke (2007) assumed it removed the oxic layer (link 4, Fig. 7). Accounting for the accumulation of sediment and particulate organic carbon in the water column after trawling, Durrieu de Madron et al. (2005) determined that otter trawls resuspended 0.1 to 0.4 mm thick layers in muddy sediments. The resuspension of much thicker layers has been estimated for fluxes of dissolved nutrients (Durrieu de Madron et al., 2005; Duplisea et al., 2001), but these studies may not have distinguished between porewater mixing and resuspension (see sect. 4.3.1).

The quantified furrow volume allows the amount of material resuspended by otter trawls to be estimated. Furrows disappear on the time scale of a year (Schönke et al., 2022). Under the assumption of steady-state ($Q = \lambda V$), where Q represents the volumetric furrow production rate by

668 trawling, λ is a constant for the furrow disappearance rate (estimated to be 1 y^{-1}), and V denotes
669 the furrow volume in a tile, the erosion can be estimated as $r = Qf/A$. Here, f denotes the ratio of
670 the resuspended layer depth over the furrow volume, and A represents the tile area. When f is 22%
671 (de Borger et al., 2021), the erosion exceeds or is on the same magnitude as the burial velocities
672 for sites 8, 10, 13, and 18. However, considering a resuspended depth layer on the order of 0.2 mm
673 for furrow depths that typically range between 15 – 30 cm in fine-grained sediment (Linnane et al.,
674 2000), this f-ratio would be only ~1%, yielding lower erosion rates that are by far exceeded by the
675 sediment burial velocities. The latter estimates agree better with our findings. Clouds of
676 resuspended materials spread horizontally over 100s of meters in the water column (e.g., Durrieu
677 de Madron et al., 2005) far outside local tiles (10 m x 10 m, Fig. 1). The net accumulation rates in
678 combination with POM fluxes that are similar at all sites and do not scale with sediment
679 accumulation rate (Table 5) are consistent with lower estimates of sediment resuspension rates, as
680 otherwise more heavily trawled locations would have lost greater amounts of reactive POM (link
681 8; Fig. 7).
682

683 ### 4.3.3. Evaluating the trawling probability at coring locations

684 Following the reasoning in the previous section, an areal trawling intensity can be estimated as
685 $G = \lambda S$ (dimensions T^{-1}), whereby λ is the constant for recovery (estimated to be 1 y^{-1}), and S is
686 the steady-state furrow area divided by the control area. The chance for a random point in the
687 control area of being ploughed one or more times during a period t is $p(t) = 1 - \exp(-Gt)$.
688 Furrows covered about 5% of the entire study area ($S = 0.05$; Schönke et al., 2022), which yields

probabilities of $p = 5\%$, 50%, and 95% corresponding to $t = 1$, 14, and 60 years, respectively. For site 13, with the highest trawling intensity index, these chances correspond to $t = 0.2$, 3, and 14 years, respectively. Hence, it is very likely that many coring locations in our study have been directly exposed to otter boards in the last decades (link 1 supported, Fig. 7).

These calculations do not consider the potential impact of the nets and ground gear on the seabed. In the acoustic data, a clear imprint of nets between tracks of otter boards could not be discerned. However, as noted by O'Neill and Ivanović (2016), the drag forces associated with the nets and ground gear can exceed those of the otter boards but are more spread out. While the likelihood of random points encountering a net is considerably higher than encountering an otter board, the nets may not visibly create furrows, and the sediment substrate likely influences the relative impact.

4.4. The influence of environmental conditions and policies on the impact of bottom-trawling on early diagenesis

Bioturbation can have similar effects as trawling by mixing and oxygenating sediment (links 2 and 5, Fig. 7) and enhancing resuspension (links 4, 6; Fig. 7). Therefore, bottom-trawling may be less disruptive in strongly bioturbated environments (Duplisea et al., 2001; de Borger et al., 2021) when the bioturbation potential remains relatively unaffected (link 3, Fig. 7).

At our study site, large *A. islandica* and a few smaller polychaetes effectively determine the reworking of sediments and can survive in the intensely trawled area. Van Denderen et al. (2022) also found that trawling did not negatively affect the abundance of other mollusk species deeper in

710 the Baltic Sea. A ban on beam trawling probably helped to reduce the impacts, as beam trawls
711 typically cause higher mortality rates than otter trawls (e.g., Lindeboom and De Groot, 1998). The
712 annual fishing mortality of mature *A. islandica* was 11% for beam trawling and <0.5% for otter
713 trawling in the southern North Sea (Bergman and van Santbrink, 2000), but Rumohr and Krost
714 (1991) observed a larger impact of otter trawling in the western Baltic. High macrofaunal
715 biomasses and low biodiversity resulting from episodic hypoxia and low salinity are typical for the
716 Baltic Sea (Bonsdorff, 2006). The low biodiversity combined with the slow reproduction of *A.*
717 *islandica* could make the system behave more stable and less adaptive to gradual changes in
718 trawling intensity and gear until thresholds for its survival, which also depend on other
719 environmental stressors (e.g., warming), are exceeded, leading potentially to more abrupt changes
720 in community composition and bioturbation potential.

721 Fishing gear regulations not only influence benthic fauna mortality and bycatch but also
722 impact sediment resuspension. Smaller mesh sizes result in larger twine areas, increasing drag
723 forces during trawling (Reid, 1977). These regulations have evolved, and variations exist across
724 different maritime zones. For instance, the Baltic Sea experienced a significant shift in regulations,
725 transitioning from the absence of minimum mesh sizes before 1950 to the current allowance of
726 only standard meshes >105 mm (Madsen, 2007). On top of environmental diversity in sediment
727 substrate and benthic fauna, the variety in fishing gear further contributes to the complexity of
728 comparing trawling impacts between studies.

729 The effects of trawling on OM storage in sediments are expected to depend on the sediment
730 accumulation rate and hydrodynamic conditions (Epstein et al., 2022). However, despite significant
731 net sediment deposition and sufficiently calm hydrodynamic conditions allowing for the

accumulation of sandy silt sediments in the study area, we observed little impact.

Conclusion

As reflected by the redox-defined zonation of microbial OM mineralization, the biogeochemical functions at all sites follow the classical pattern of vertical redox stratification (Froelich et al., 1979). Observed and modeled differences in bioturbation and sedimentation rates explain most variability in early diagenetic transformation rates at the study sites. A direct link between trawling intensities and net sediment accumulation rates could not be established. The same model-constrained mineralization rates at all sites indicate limited loss of reactive OM due to trawling-induced resuspension. The effect of bottom-trawling on bioturbation potentials and the macrofaunal community was found to be very limited, even at locations with high trawling intensity. Trawling intensities could not be clearly associated with biogeochemical features, and it is likely that the trawling impact was diminished by the stronger disturbance caused by persistent bioturbation.

The results in this study challenge the initial predictions based on environmental parameters. Despite the high vulnerability of *A. islandica* to bottom-trawling, as indicated in the literature (sect. 4.2), they exhibited resilience and dominated the biomass. Additionally, it was anticipated that bottom-trawling would have a more significant impact on the biogeochemistry, considering the positive net deposition of sediment and the finer sediment substrate prone to resuspension. The effects of bottom-trawling on early diagenesis appear to be highly contingent upon the local environment and its macrofauna, which are also exposed to other anthropogenic and

753 natural stressors, particularly in estuaries, marginal seas, and coastal areas. To gain a
754 comprehensive understanding of the trawling impact and enable general estimations, it is essential
755 to account for the variability in site-specific conditions. Unfortunately, there is a scarcity of
756 empirical biogeochemical studies, as highlighted in the compilation by Epstein et al. (2022), where
757 only seven studies reported the effects of trawling on benthic mineralization. Therefore, it is crucial
758 to conduct further investigations across diverse environments to evaluate the long-term impact of
759 bottom-trawling on early diagenesis and sediment carbon storage.
760

761 ## Author contributions

762 JR performed the modeling and wrote the first draft of the manuscript. MZ conducted fieldwork
763 and supervised geochemical analyses. MG contributed to fieldwork and conducted the macrofaunal
764 analysis. PR conducted associated fieldwork and performed geochemical analyses. JK contributed
765 the SRR measurements. MS contributed to fieldwork and worked on acoustics. HR and MEB led
766 the modeling and biogeochemical parts of the project, respectively. All authors were involved in
767 discussing the results, read the manuscript, and contributed by writing and editing. All (co)authors
768 agree with the submission in the present form.
769

770 ## Acknowledgements

771 This work was conducted within the DAM pilot mission "MGF-Ostsee" (Grant No. 03F0848A)
772 funded by the German Federal Ministry of Education and Research. The carbon cycle part of the
773 study further contributes to the BMBF project COOLSTYLE as part of CARBOSTORE. The

authors would like to express their gratitude to I. Scherff, I. Schmiedinger, A. Köhler, and the student helpers for their valuable contributions in conducting the chemical analyses. Sincere appreciation is also extended to captains D. Thürsam and T. Kaufmann, their officers, and the dedicated crew of the R/V Elisabeth Mann Borgese for their hospitality and support throughout the EMB238 and EMB267 cruises.

References

Al-Raei, A.M., Bosselmann, K., Böttcher, M.E., Hespenheide, B., Tauber, F., 2009. Seasonal dynamics of microbial sulfate reduction in temperate intertidal surface sediments: controls by temperature and organic matter. Ocean Dynamics 59, 351–370. doi:10.1007/s10236-009-0186-5.

Allen, J., Clarke, K., 2007. Effects of demersal trawling on ecosystem functioning in the north sea: a modelling study. Marine Ecology Progress Series 336, 63–75. doi:10.3354/meps336063.

Amoroso, R.O., Pitcher, C.R., Rijnsdorp, A.D., McConnaughey, R.A., Parma, A.M., Suuronen, P., Eigaard, O.R., Bastardie, F., Hintzen, N.T., Althaus, F., et al., 2018. Bottom trawl fishing footprints on the world's continental shelves. Proceedings of the National Academy of Sciences 115, E10275–E10282. doi:10.1073/pnas.1802379115.

Arndt, S., Jørgensen, B., LaRowe, D., Middelburg, J., Pancost, R., Regnier, P., 2013. Quantifying the degradation of organic matter in marine sediments: A review and synthesis. Earth-Science Reviews 123, 53–86. doi:10.1016/j.earscirev.2013.02.008.

von Arntz, W.E., Weber, W., 1970. Cyprina islandica l.(mollusca, bivalvia) als nahrung von dorsch

795 und kliesche in der kieler bucht. Berichte der Deutschen Wissenschaftlichen Kommission
796 für Meeresforschung 21, 193–209.

797 Atwood, T.B., Sala, E., Mayorga, J., Bradley, D., Cabral, R.B., Auber, A., Cheung, W., Ferretti, F.,
798 Friedlander, A.M., Gaines, S.D., Garilao, C., Goodell, W., Halpern, B.S., Hinson, A.,
799 Kaschner, K., KesnerReyes, K., Leprieur, F., McGowan, J., Morgan, L.E., Mouillot, D.,
800 Palacios-Abrantes, J., Possingham, H.P., Rechberger, K.D., Worm, B., Lubchenco, J., 2023.
801 Reply to: Quantifying the carbon benefits of ending bottom trawling. Nature 617, E3–E5.
802 doi:10.1038/s41586-023-06015-6.

803 Baltic Sea Hydrographic Commission, 2013. Baltic sea bathymetry database version 0.9.3.
804 http://data.bshc.pro/. Accessed: 2023-05-26.

805 Bastardie, F., Brown, E.J., Andonegi, E., Arthur, R., Beukhof, E., Depestele, J., Döring, R., Eigaard,
806 O.R., García-Barón, I., Llope, M., Mendes, H., Piet, G., Reid, D., 2021. A review
807 characterizing 25 ecosystem challenges to be addressed by an ecosystem approach to
808 fisheries management in europe. Frontiers in Marine Science 7.
809 doi:10.3389/fmars.2020.629186.

810 Berg, P., Rysgaard, S., Thamdrup, B., 2003. Dynamic modeling of early diagenesis and nutrient
811 cycling. a case study in an artic marine sediment. American Journal of Science 303, 905–
812 955. doi:10.2475/ajs.303.10.905.

813 Bergman, M.J., van Santbrink, J.W., 2000. Mortality in megafaunal benthic populations caused by
814 trawl fisheries on the dutch continental shelf in the north sea in 1994. ICES Journal of
815 Marine Science 57, 1321–1331. doi:10.1006/jmsc.2000.0917.

816 Berner, R.A., 1980. Early diagenesis: a theoretical approach. 1, Princeton University Press.

doi:10.2307/j.ctvx8b6p2.

Berner, R.A., 1982. Burial of organic carbon and pyrite sulfur in the modern ocean: its geochemical and environmental significance. American Journal of Science 282. doi:10.2475/ajs.282.4.451.

Bhagirathan, U., Meenakumari, B., Jayalakshmy, K.V., Panda, S.K., Madhu, V.R., Vaghela, D.T., 2008. Impact of bottom trawling on sediment characteristics—a study along inshore waters off veraval coast, india. Environmental Monitoring and Assessment 160, 355–369. doi:10.1007/s10661-008-0700-0.

Bonsdorff, E., 2006. Zoobenthic diversity-gradients in the baltic sea: Continuous post-glacial succession in a stressed ecosystem. Journal of Experimental Marine Biology and Ecology 330, 383–391. doi:10.1016/j. jembe.2005.12.041.

de Borger, E., Tiano, J., Braeckman, U., Rijnsdorp, A.D., Soetaert, K., 2021. Impact of bottom trawling on sediment biogeochemistry: a modelling approach. Biogeosciences 18, 2539–2557. doi:10.5194/bg-182539-2021.

Boudreau, B.P., 1997. Diagenetic models and their implementation. volume 505. Springer Berlin. doi:10.1007/978-3-642-60421-8.

Boudreau, B.P., 2005. Modelling mixing and diagenesis, in: Coastal and Estuarine Studies. American Geophysical Union, pp. 323–340. doi:10.1029/ce060p0323.

Bradshaw, C., Jakobsson, M., Brüchert, V., Bonaglia, S., Mörth, C.M., Muchowski, J., Stranne, C., Sköld, M., 2021. Physical disturbance by bottom trawling suspends particulate matter and alters biogeochemical processes on and near the seafloor. Frontiers in Marine Science 8.

doi:10.3389/fmars.2021.683331.

BSH, 2016. Anleitung zur kartierung des meeresbodens mittels hochauflösender sonare in den deutschen meeresgebieten. bsh nr. 7201, s. 33. https://www.bsh.de/download/Kartierung-des-Meeresboden.pdf.

Böttcher, M.E., Hespenheide, B., Llobet-Brossa, E., Beardsley, C., Larsen, O., Schramm, A., Wieland, A., Böttcher, G., Berninger, U.G., Amann, R., 2000. The biogeochemistry, stable isotope geochemistry, and microbial community structure of a temperate intertidal mudflat: an integrated study. Continental Shelf Research 20, 1749–1769. doi:10.1016/s0278-4343(00)00046-7.

Cline, J.D., 1969. Spectrophotometric determination of hydrogen sulfide in natural waters 1. Limnology and Oceanography 14, 454–458. doi:10.4319/lo.1969.14.3.0454.

van Denderen, P., Törnroos, A., Sciberras, M., Hinz, H., Friedland, R., Lasota, R., Mangano, M., Robertson, C., Valanko, S., Hiddink, J., 2022. Effects of bottom trawling and hypoxia on benthic invertebrate communities. Marine Ecology Progress Series 694, 13–27. doi:10.3354/meps14094.

Downie, A., Noble-James, T., Chaverra, A., Howell, K., 2021. Predicting sea pen (pennatulacea) distribution on the UK continental shelf: evidence of range modification by benthic trawling. Marine Ecology Progress Series 670, 75–91. doi:10.3354/meps13744.

Duplisea, D.E., Jennings, S., Malcolm, S.J., Parker, R., Sivyer, D.B., 2001. Modelling potential impacts of bottom trawl fisheries on soft sediment biogeochemistry in the north sea. Geochemical Transactions 2. doi:10.1186/1467-4866-2-112.

Durrieu de Madron, X., Ferré, B., Corre, G.L., Grenz, C., Conan, P., Pujo-Pay, M., Buscail, R., Bodiot, O., 2005. Trawling-induced resuspension and dispersal of muddy sediments and dissolved elements in the gulf of lion (NW mediterranean). Continental Shelf Research 25, 2387–2409. doi:10.1016/j.csr.2005.08.002.

Eigaard, O.R., Bastardie, F., Breen, M., Dinesen, G.E., Hintzen, N.T., Laffargue, P., Mortensen, L.O., Nielsen, J.R., Nilsson, H.C., O'Neill, F.G., Polet, H., Reid, D.G., Sala, A., Sköld, M., Smith, C., Sørensen, T.K., Tully, O., Zengin, M., Rijnsdorp, A.D., 2015. Estimating seabed pressure from demersal trawls, seines, and dredges based on gear design and dimensions. ICES Journal of Marine Science 73, i27–i43. doi:10.1093/icesjms/fsv099.

Epstein, G., Middelburg, J.J., Hawkins, J.P., Norris, C.R., Roberts, C.M., 2022. The impact of mobile demersal fishing on carbon storage in seabed sediments. Global Change Biology 28, 2875–2894. doi:10.1111/gcb.16105.

FEMA, 2013. Fehmarnbelt fixed link eia. marine fauna and flora – baseline. benthic fauna of the fehmarnbelt area. report no. e2tr0020.

Ferguson, A.J.P., Oakes, J., Eyre, B.D., 2020. Bottom trawling reduces benthic denitrification and has the potential to influence the global nitrogen cycle. Limnology and Oceanography Letters 5, 237–245. doi:10.1002/lol2.10150.

Fossing, H., Jørgensen, B.B., 1989. Measurement of bacterial sulfate reduction in sediments: Evaluation of a single-step chromium reduction method. Biogeochemistry 8. doi:10.1007/bf00002889.

Friedland, R., Vock, C., Piehl, S., 2023. Estimation of hypoxic areas in the western baltic sea with geostatistical models. Water, 15, 3235. doi:10.3390/w15183235.

Froelich, P., Klinkhammer, G., Bender, M., Luedtke, N., Heath, G., Cullen, D., Dauphin, P., Hammond, D., Hartman, B., Maynard, V., 1979. Early oxidation of organic matter in pelagic sediments of the eastern equatorial atlantic: suboxic diagenesis. Geochimica et Cosmochimica Acta 43, 1075–1090. doi:10.1016/0016-7037(79)90095-4.

Gogina, M., Darr, A., Zettler, M.L., 2014. Approach to assess consequences of hypoxia disturbance events for benthic ecosystem functioning. Journal of Marine Systems 129, 203–213. doi:10.1016/j.jmarsys.2013.06.001.

Gogina, M., Zettler, M.L., Vanaverbeke, J., Dannheim, J., Hoey, G.V., Desroy, N., Wrede, A., Reiss, H., Degraer, S., Lancker, V.V., Foveau, A., Braeckman, U., Fiorentino, D., Holstein, J., Birchenough, S.N., 2020. Interregional comparison of benthic ecosystem functioning: Community bioturbation potential in four regions along the NE atlantic shelf. Ecological Indicators 110, 105945. doi:10.1016/j.ecolind.2019.105945.

HELCOM Red List Biotope Expert Group, 2019. Biotope information sheet. https://helcom.fi/wpcontent/uploads/2019/08/HELCOM-Red-List-AB.H3L3.pdf. Accessed: 2023-03-07.

Hiddink, J.G., van de Velde, S.J., McConnaughey, R.A., de Borger, E., Tiano, J., Kaiser, M.J., Sweetman, A.K., Sciberras, M., 2023. Quantifying the carbon benefits of ending bottom trawling. Nature 617, E1–E2.doi:10.1038/s41586-023-06014-7.

Hindmarsh, A.C., Brown, P.N., Grant, K.E., Lee, S.L., Serban, R., Shumaker, D.E., Woodward, C.S., 2005. SUNDIALS. ACM Transactions on Mathematical Software 31, 363–396. doi:10.1145/1089014.1089020.

Hintzen, N.T., Aarts, G., Poos, J.J., der Reijden, K.J.V., Rijnsdorp, A.D., 2020. Quantifying habitat

903 preference of bottom trawling gear. ICES Journal of Marine Science 78, 172–184.
904 doi:10.1093/icesjms/fsaa207.

905 Hir, P.L., Monbet, Y., Orvain, F., 2007. Sediment erodability in sediment transport modelling: Can
906 we account for biota effects? Continental Shelf Research 27, 1116–1142.
907 doi:10.1016/j.csr.2005.11.016.

908 Hofmann, A.F., Soetaert, K., Middelburg, J.J., Meysman, F.J.R., 2010. AquaEnv : An aqua tic acid–
909 base modelling env ironment in r. Aquatic Geochemistry 16, 507–546. doi:10.1007/s10498-
910 009-9084-1.

911 Hollweg, T., Gilmour, C., Mason, R., 2009. Methylmercury production in sediments of chesapeake
912 bay and the mid-atlantic continental margin. Marine Chemistry 114, 86–101.
913 doi:10.1016/j.marchem.2009.04.004.

914 ICES, 2021a. Baltic Fisheries Assesment Working Group (WGBFAS). ICES Scientific Reports.
915 https://ices-library.figshare.com/articles/report/Baltic_Fisheries_Assesment_Working_
916 Group_WGBFAS_/18618875. doi:10.17895/ices.pub.8187.

917 ICES, 2021b. Cod (Gadus morhua) in subdivisions 24–32, eastern Baltic stock (eastern Baltic
918 Sea), ICES Advice: Recurrent Advice. https://ices-
919 library.figshare.com/articles/report/Cod_Gadus_
920 morhua_in_subdivisions_24_32_eastern_Baltic_stock_eastern_Baltic_Sea_/18638282.
921 doi:10.17895/ices.advice.7745.

922 Jørgensen, B.B., 1978. A comparison of methods for the quantification of bacterial sulfate reduction
923 in coastal marine sediments. Geomicrobiology Journal 1, 11–27.
924 doi:10.1080/01490457809377721.

925 Kaiser, M., Clarke, K., Hinz, H., Austen, M., Somerfield, P., Karakassis, I., 2006. Global analysis
926 of response and recovery of benthic biota to fishing. Marine Ecology Progress Series 311,
927 1–14. doi:10.3354/meps311001.

928 Kaiser, M.J., 1998. Significance of bottom-fishing disturbance. Conservation Biology 12, 1230–
929 1235. doi:10.1046/j.1523-1739.1998.0120061230.x.

930 Kallmeyer, J., Ferdelman, T.G., Weber, A., Fossing, H., Jørgensen, B.B., 2004. A cold chromium
931 distillation procedure for radiolabeled sulfide applied to sulfate reduction measurements.
932 Limnology and Oceanography: Methods 2, 171–180. doi:10.4319/lom.2004.2.171.

933 Keil, R.G., Montluçon, D.B., Prahl, F.G., Hedges, J.I., 1994. Sorptive preservation of labile organic
934 matter in marine sediments. Nature 370, 549–552. doi:10.1038/370549a0.

935 Kowalski, N., Dellwig, O., Beck, M., Grunwald, M., Fischer, S., Piepho, M., Riedel, T., Freund,
936 H., Brumsack, H.J., Böttcher, M.E., 2009. Trace metal dynamics in the water column and
937 pore waters in a temperate tidal system: response to the fate of algae-derived organic matter.
938 Ocean Dynamics 59, 333–350. doi:10.1007/s10236-009-0192-7.

939 Kristensen, E., Penha-Lopes, G., Delefosse, M., Valdemarsen, T., Quintana, C., Banta, G., 2012.
940 What is bioturbation? the need for a precise definition for fauna in aquatic sciences. Marine
941 Ecology Progress Series 446, 285–302. doi:10.3354/meps09506.

942 Leipe, T., Moros, M., Kotilainen, A., Vallius, H., Kabel, K., Endler, M., Kowalski, N., 2013.
943 Mercury in baltic sea sediments—natural background and anthropogenic impact.
944 Geochemistry 73, 249–259. doi:10.1016/j.chemer.2013.06.005.

945 Lindeboom, H., De Groot, S., 1998. The effects of different types of fisheries on the North Sea and

Irish Sea benthic ecosystems. C003/98. Impact-II: NIOZ-rapport 1998-1.

Linnane, A., Ball, B., Munday, B., Van Marlen, B., Bergman, M., Fonteyne, R., 2000. A review of potential techniques to reduce the environmental impact of demersal trawls. Irish Fisheries Investigations (New Series) 7, 1–39.

Lipka, M., Woelfel, J., Gogina, M., Kallmeyer, J., Liu, B., Morys, C., Forster, S., Böttcher, M.E., 2018. Solute reservoirs reflect variability of early diagenetic processes in temperate brackish surface sediments. Frontiers in Marine Science 5. doi:10.3389/fmars.2018.00413.

Luff, R., Wallmann, K., 2003. Fluid flow, methane fluxes, carbonate precipitation and biogeochemical turnover in gas hydrate-bearing sediments at hydrate ridge, cascadia margin: numerical modeling and mass balances. Geochimica et Cosmochimica Acta 67, 3403–3421. doi:10.1016/s0016-7037(03)00127-3.

Luisetti, T., Turner, R.K., Andrews, J.E., Jickells, T.D., Kröger, S., Diesing, M., Paltriguera, L., Johnson, M.T., Parker, E.R., Bakker, D.C., Weston, K., 2019. Quantifying and valuing carbon flows and stores in coastal and shelf ecosystems in the UK. Ecosystem Services 35, 67–76. doi:10.1016/j.ecoser.2018.10.013.

Madsen, N., 2007. Selectivity of fishing gears used in the baltic sea cod fishery. Reviews in Fish Biology and Fisheries 17, 517–544. doi:10.1007/s11160-007-9053-y.

Mayer, L.M., 1994. Relationships between mineral surfaces and organic carbon concentrations in soils and sediments. Chemical Geology 114, 347–363. doi:10.1016/0009-2541(94)90063-9.

Mazor, T., Pitcher, C.R., Rochester, W., Kaiser, M.J., Hiddink, J.G., Jennings, S., Amoroso, R.,

McConnaughey, R.A., Rijnsdorp, A.D., Parma, A.M., Suuronen, P., Collie, J., Sciberras, M., Atkinson, L., Durholtz, D., Ellis, J.R., Bolam, S.G., Schratzberger, M., Couce, E., Eggleton, J., Garcia, C., Kainge, P., Paulus, S., Kathena, J.N., Gogina, M., van Denderen, P.D., Keller, A.A., Horness, B.H., Hilborn, R., 2020. Trawl fishing impacts on the status of seabed fauna in diverse regions of the globe. Fish and Fisheries 22, 72–86. doi:10.1111/faf.12506.

McLaverty, C., Eigaard, O.R., Gislason, H., Bastardie, F., Brooks, M.E., Jonsson, P., Lehmann, A., Dinesen, G.E., 2020. Using large benthic macrofauna to refine and improve ecological indicators of bottom trawling disturbance. Ecological Indicators 110, 105811. doi:10.1016/j.ecolind.2019.105811.

Meile, C., Cappellen, P.V., 2003. Global estimates of enhanced solute transport in marine sediments. Limnology and Oceanography 48, 777–786. doi:10.4319/lo.2003.48.2.0777.

Meister, P., Liu, B., Khalili, A., Böttcher, M.E., Jørgensen, B.B., 2019. Factors controlling the carbon isotope composition of dissolved inorganic carbon and methane in marine porewater: An evaluation by reactiontransport modelling. Journal of Marine Systems 200, 103227. doi:10.1016/j.jmarsys.2019.103227.

Meysman, F.J.R., Boudreau, B.P., Middelburg, J.J., 2003. Relations between local, nonlocal, discrete and continuous models of bioturbation. Journal of Marine Research 61, 391–410. doi:10.1357/002224003322201241.

Middelburg, J.J., Soetaert, K., Herman, P.M., 1997. Empirical relationships for use in global diagenetic models. Deep Sea Research Part I: Oceanographic Research Papers 44, 327–344. doi:10.1016/S09670637(96)00101-X.

Morys, C., Brüchert, V., Bradshaw, C., 2021. Impacts of bottom trawling on benthic biogeochemistry in muddy sediments: Removal of surface sediment using an experimental field study. Marine Environmental Research 169, 105384. doi:10.1016/j.marenvres.2021.105384.

Muench, A., DePiper, G.S., Demarest, C., 2018. On the precision of predicting fishing location using data from the vessel monitoring system (VMS). Canadian Journal of Fisheries and Aquatic Sciences 75, 1036– 1047. doi:10.1139/cjfas-2016-0446.

Naumov, L., Neumann, T., Radtke, H., Meier, H.E.M., 2023. Limited ventilation of the central baltic sea due to elevated oxygen consumption. Frontiers in Marine Science 10. doi:10.3389/fmars.2023.1175643.

Nielsen, J.R., Vastenhoud, B.M., Bossier, S., Møhlenberg, F., Christensen, A., Diekman, R., Dinesen, G.E., Eigaard, O.R., Gogina, M., Zettler, M.L., Darr, A., Bastardie, F., 2023. Impacts of habitat-specific benthic fishing compared to those of short-term induced variability by environmental drivers in a turbulent baltic sea environment. Fisheries Research 257, 106514. doi:10.1016/j.fishres.2022.106514.

Oberle, F.K., Swarzenski, P.W., Reddy, C.M., Nelson, R.K., Baasch, B., Hanebuth, T.J., 2016. Deciphering the lithological consequences of bottom trawling to sedimentary habitats on the shelf. Journal of Marine Systems 159, 120–131. doi:10.1016/j.jmarsys.2015.12.008.

Olsgard, F., Schaanning, M.T., Widdicombe, S., Kendall, M.A., Austen, M.C., 2008. Effects of bottom trawling on ecosystem functioning. Journal of Experimental Marine Biology and Ecology 366, 123–133. doi:10.1016/j.jembe.2008.07.036.

O'Neill, F., Summerbell, K., 2011. The mobilisation of sediment by demersal otter trawls. Marine

Pollution Bulletin 62, 1088–1097. doi:10.1016/j.marpolbul.2011.01.038.

O'Neill, F.G., Ivanović, A., 2016. The physical impact of towed demersal fishing gears on soft sediments. ICES Journal of Marine Science 73, i5–i14. doi:10.1093/icesjms/fsv125.

Palanques, A., Guillén, J., Puig, P., 2001. Impact of bottom trawling on water turbidity and muddy sediment of an unfished continental shelf. Limnology and Oceanography 46, 1100–1110. doi:10.4319/lo.2001.46.5.1100.

Paradis, S., Goñi, M., Masqué, P., Durán, R., Arjona-Camas, M., Palanques, A., Puig, P., 2021. Persistence of biogeochemical alterations of deep-sea sediments by bottom trawling. Geophysical Research Letters 48, e2020GL091279. doi:10.1029/2020GL091279.

Paradis, S., Pusceddu, A., Masqué, P., Puig, P., Moccia, D., Russo, T., Iacono, C.L., 2019. Organic matter contents and degradation in a highly trawled area during fresh particle inputs (gulf of castellammare, southwestern mediterranean). Biogeosciences 16, 4307–4320. doi:10.5194/bg-16-4307-2019.

Polymenakou, P.N., Pusceddu, A., Tselepides, A., Polychronaki, T., Giannakourou, A., Fiordelmondo, C., Hatziyanni, E., Danovaro, R., 2005. Benthic microbial abundance and activities in an intensively trawled ecosystem (thermaikos gulf, aegean sea). Continental Shelf Research 25, 2570–2584. doi:10.1016/j.csr.2005.08.018.

Pusceddu, A., Bianchelli, S., Martín, J., Puig, P., Palanques, A., Masqué, P., Danovaro, R., 2014. Chronic and intensive bottom trawling impairs deep-sea biodiversity and ecosystem functioning. Proceedings of the National Academy of Sciences 111, 8861–8866. doi:10.1073/pnas.1405454111.

1032 Pusceddu, A., Fiordelmondo, C., Polymenakou, P., Polychronaki, T., Tselepides, A., Danovaro, R.,
1033 2005. Effects of bottom trawling on the quantity and biochemical composition of organic
1034 matter in coastal marine sediments (thermaikos gulf, northwestern aegean sea). Continental
1035 Shelf Research 25, 2491–2505. doi:10.1016/j.csr.2005.08.013.
1036 Queirós, A., Hiddink, J., Kaiser, M., Hinz, H., 2006. Effects of chronic bottom trawling disturbance
1037 on benthic biomass, production and size spectra in different habitats. Journal of
1038 Experimental Marine Biology and Ecology 335, 91–103. doi:10.1016/j.jembe.2006.03.001.
1039 R Core Team, 2022. R: A Language and Environment for Statistical Computing. R Foundation for
1040 Statistical Computing. Vienna, Austria. URL: https://www.R-project.org/.
1041 Raiswell, R., Canfield, D.E., 2012. The iron biogeochemical cycle past and present. Geochemical
1042 Perspectives 1, 1–220. doi:10.7185/geochempersp.1.1.
1043 Reid, A.J., 1977. A net drag formula for pelagic nets. Scottish Fisheries Research Report No. 7.
1044 Rickard, D., Luther, G.W.I., 2007. Chemistry of iron sulfides. ChemInform 38.
1045 doi:10.1002/chin.200719200.
1046 Rooze, J., Peterson, L., Peterson, R.N., Meile, C., 2020. Porewater flow patterns in surficial cold
1047 seep sediments inferred from conservative tracer profiles and early diagenetic modeling.
1048 Chemical Geology 536, 119468. doi:10.1016/j.chemgeo.2020.119468.
1049 Rullkötter, J., 2006. Organic matter: The driving force for early diagenesis, in: Schulz, H.D., Zabel,
1050 M. (Eds.), Marine Geochemistry. Springer Berlin Heidelberg, Berlin, Heidelberg, pp. 125–
1051 168. doi:10.1007/3-540-32144-6_4.
1052 Rumohr, H., Krost, P., 1991. Experimental evidence of damage to benthos by bottom trawling with

special reference to arctica islandica. Meeresforschung - Reports on Marine Research 33, 340–345. URL: https://oceanrep.geomar.de/id/eprint/42238/.

Sala, E., Mayorga, J., Bradley, D., Cabral, R.B., Atwood, T.B., Auber, A., Cheung, W., Costello, C., Ferretti, F., Friedlander, A.M., Gaines, S.D., Garilao, C., Goodell, W., Halpern, B.S., Hinson, A., Kaschner, K., Kesner-Reyes, K., Leprieur, F., McGowan, J., Morgan, L.E., Mouillot, D., Palacios-Abrantes, J., Possingham, H.P., Rechberger, K.D., Worm, B., Lubchenco, J., 2021. Protecting the global ocean for biodiversity, food and climate. Nature 592, 397–402. doi:10.1038/s41586-021-03371-z.

Schacht, K., Voss, R., 2022. German fishery's adaptation to historic events, western baltic sea, 1890–1950. Ambio 52, 155–170. doi:10.1007/s13280-022-01768-2.

Schaller, J., 2014. Bioturbation/bioirrigation by chironomus plumosus as main factor controlling elemental remobilization from aquatic sediments? Chemosphere 107, 336–343. doi:10.1016/j.chemosphere.2013.12.086.

Schönke, M., Clemens, D., Feldens, P., 2022. Quantifying the physical impact of bottom trawling based on high-resolution bathymetric data. Remote Sensing 14, 2782. doi:10.3390/rs14122782.

Slomp, C., der Gaast, S.V., Raaphorst, W.V., 1996. Phosphorus binding by poorly crystalline iron oxides in north sea sediments. Marine Chemistry 52, 55–73. doi:10.1016/0304-4203(95)00078-x.

Smith, C., Papadopoulou, K., Diliberto, S., 2000. Impact of otter trawling on an eastern mediterranean commercial trawl fishing ground. ICES Journal of Marine Science 57, 1340–1351. doi:10.1006/jmsc.2000.0927.

1075 Soetaert, K., Meysman, F., 2012. Reactive transport in aquatic ecosystems: Rapid model
1076 prototyping in the open source software r. Environmental Modelling & Software 32, 49–
1077 60. doi:10.1016/j.envsoft.2011.08.011.

1078 Solan, M., Cardinale, B.J., Downing, A.L., Engelhardt, K.A.M., Ruesink, J.L., Srivastava, D.S.,
1079 2004. Extinction and ecosystem function in the marine benthos. Science 306, 1177–1180.
1080 doi:10.1126/science.1103960.

1081 Steefel, C.I., MacQuarrie, K.T.B., 1996. Chapter 2. approaches to modeling of reactive transport
1082 in porous media, in: Reactive Transport in Porous Media. De Gruyter, pp. 83–130.
1083 doi:10.1515/9781501509797005.

1084 Tauber, F., 2012. Meeresbodenrelief in der deutschen ostsee: Fehmarn, karte nr. 2942/seabed relief
1085 in the german baltic sea: Fehmarn, map no. 2942. Bundesamt für Seeschifffahrt und
1086 Hydrographie. Hamburg, Germany. ISBN 978 3 86987 390 9.

1087 Taylor, A.C., 1976. Burrowing behaviour and anaerobiosis in the bivalve Arctica islandica (l.).
1088 Journal of the Marine Biological Association of the United Kingdom 56, 95–109.
1089 doi:10.1017/s0025315400020464.

1090 Thompson, I., Jones, D.S., Dreibelbis, D., 1980a. Annual internal growth banding and life history
1091 of the ocean quahog arctica islandica (mollusca: Bivalvia). Marine Biology 57, 25–34.
1092 doi:10.1007/bf00420964.

1093 Thompson, I., Jones, D.S., Ropes, J.W., 1980b. Advanced age for sexual maturity in the ocean
1094 quahog arctica islandica (mollusca: Bivalvia). Marine Biology 57, 35–39.
1095 doi:10.1007/bf00420965.

1096 Thullner, M., Dale, A.W., Regnier, P., 2009. Global-scale quantification of mineralization pathways
1097 in marine sediments: A reaction-transport modeling approach. Geochemistry, Geophysics,
1098 Geosystems 10. doi:10.1029/2009GC002484.

1099 Tiano, J.C., Depestele, J., Hoey, G.V., Fernandes, J., van Rijswijk, P., Soetaert, K., 2022. Trawling
1100 effects on biogeochemical processes are mediated by fauna in high-energy biogenic-reef-
1101 inhabited coastal sediments. Biogeosciences 19, 2583–2598. doi:10.5194/bg-19-2583-
1102 2022.

1103 Tyler-Walters, H., Sabatini, M., 2017. Icelandic cyprine (Arctica islandica), in: Tyler-Walters, H.,
1104 Hiscock, K. (Eds.), Marine Life Information Network: Biology and Sensitivity Key
1105 Information Reviews, [online]. Plymouth: Marine Biological Association of the United
1106 Kingdom, pp. 1–32. doi:10.17031/marlinsp.1519.2.

1107 Vaquer-Sunyer, R., Duarte, C.M., 2010. Sulfide exposure accelerates hypoxia-driven mortality.
1108 Limnology and Oceanography 55, 1075–1082. doi:10.4319/lo.2010.55.3.1075.

1109 van de Velde, S., Lancker, V.V., Hidalgo-Martinez, S., Berelson, W.M., Meysman, F.J.R., 2018.
1110 Anthropogenic disturbance keeps the coastal seafloor biogeochemistry in a transient state.
1111 Scientific Reports 8. doi:10.1038/s41598-018-23925-y.

1112 Von Ahn, C.M.E., Scholten, J.C., Malik, C., Feldens, P., Liu, B., Dellwig, O., Jenner, A.K.,
1113 Papenmeier, S., Schmiedinger, I., Zeller, M.A., Böttcher, M.E., 2021. A multi-tracer study
1114 of fresh water sources for a temperate urbanized coastal bay (southern baltic sea). Frontiers
1115 in Environmental Science 9. doi:10.3389/fenvs.2021.642346.

1116 Wang, Y., Van Cappellen, P., 1996. A multicomponent reactive transport model of early diagenesis:
1117 Application to redox cycling in coastal marine sediments. Geochimica et Cosmochimica

Acta 60, 2993–3014. doi:10.1016/0016-7037(96)00140-8.

Warnken, K.W., Gill, G.A., Dellapenna, T.M., Lehman, R.D., Harper, D.E., Allison, M.A., 2003. The effects of shrimp trawling on sediment oxygen consumption and the fluxes of trace metals and nutrients from estuarine sediments. Estuarine, Coastal and Shelf Science 57, 25–42. doi:10.1016/s0272-7714(02)00316-5.

Watling, L., Findlay, R.H., Mayer, L.M., Schick, D.F., 2001. Impact of a scallop drag on the sediment chemistry, microbiota, and faunal assemblages of a shallow subtidal marine benthic community. Journal of Sea Research 46, 309–324. doi:10.1016/s1385-1101(01)00083-1.

Winde, V., Böttcher, M., Escher, P., Böning, P., Beck, M., Liebezeit, G., Schneider, B., 2014. Tidal and spatial variations of DI13c and aquatic chemistry in a temperate tidal basin during winter time. Journal of Marine Systems 129, 396–404. doi:10.1016/j.jmarsys.2013.08.005.

WoRMS Editorial Board, 2020. World register of marine species. https://www.marinespecies.org/.

Zacharia, P., Anoop, A., Durgekar, N.R., Krishnakumar, P., 2006. Immediate effects of experimental otter trawling on the physico-chemical parameters of seawater off mangalore. Journal of the Marine Biological Association of India 48, 200–205.

Zettler, M., Bönsch, R., Gosselck, F., 2001. Distribution, abundance and some population characteristics of the ocean quahog, arctica islandica (linnaeus, 1767), in the mecklenburg bight (baltic sea). Journal of Shellfish Research 20, 161–169.

Zindorf, M., Rooze, J., Meile, C., März, C., Jouet, G., Newton, R., Brandily, C., Pastor, L., 2021. The evolution of early diagenetic processes at the mozambique margin during the last

glacial-interglacial transition. Geochimica et Cosmochimica Acta 300, 79–94. doi:10.1016/j.gca.2021.02.024.

Tables

Table 1: Model state variables

Chemical	Notation	Type
Total reduced nitrogen*	NH_4^+	Solute
Phosphate	PO_4^{3-}	Solute
Light dissolved inorganic carbon*	$DI^{12}C$	Solute
Heavy dissolved inorganic carbon*	$DI^{13}C$	Solute
Calcium	Ca^{2+}	Solute
Iron(II)	Fe^{2+}	Solute
Manganese(II)	Mn^{2+}	Solute
Oxygen	O_2	Solute
Nitrate	NO_3^-	Solute
Sulfate	SO_4^{2-}	Solute
Total dissolved sulfide*	H_2S	Solute
Total alkalinity*	TA	Solute
Particulate organic matter*	POM	Solid
Manganese(IV) oxide†	$MnO_2^{\alpha,\beta}$	Solid
Iron(III) oxide-hydroxide†,‡	$Fe(OH)_3^{\alpha,\beta}$	Solid
Ironmonosulfide	FeS	Solid
Pyrite	FeS_2	Solid
Polysulfide	S_0	Solid
Light calcium carbonate	$Ca^{12}CO_3$	Solid
Heavy calcium carbonate	$Ca^{13}CO_3$	Solid

*Chemical definitions for equilibrium acid-base chemistry: $NH_4^+ = [NH_4^+] + [NH_3]$; DIC = $[H_2CO_3] + [HCO_3^-] + [CO_3^{2-}]$; $H_2S = [H_2S] + [HS^-]$; $TA = [HCO_3^-] + 2\,[CO_3^{2-}] + [NH_4^+] + [HS^-] + [B(OH)_4^-] + [OH^-] - [H_3O^+]$. POM is defined as $(CH_2O)_a(NH_4)_b(PO_4)_c$, whereby the a:b:c ratio is set to 122:16:1. †For metal oxides, superscript α and β indicate separate state variables denoting different mineralogies. Only the reduction of α-phases (i.e., $Fe(OH)_3^{\alpha}$ and MnO_2^{α}) can be coupled to POM mineralization. ‡Phosphate is adsorbed to $Fe(OH)_3$ in a fixed Fe:P ratio of 10:1 (Slomp et al., 1996).

Table 2: Reaction network

R_1	$\mathrm{POM} + a\ \mathrm{O_2} \rightarrow a\ (1-f)\ {}^{12}\mathrm{CO_2} + af\ {}^{13}\mathrm{CO_2} + a\ \mathrm{H_2O} + b\ \mathrm{NH_4^+} + c\ \mathrm{PO_4^{3-}}$
R_2	$\mathrm{POM} + 0.8\mathrm{a}\ \mathrm{NO_3^-} \rightarrow a\ (1-f)\ {}^{12}\mathrm{CO_2} + a\ f\ {}^{13}\mathrm{CO_2} + 0.6a\ \mathrm{H_2O} + b\ \mathrm{NH_4^+} + c\ \mathrm{PO_4^{3-}} + 0.4\ \mathrm{N_2} + 0.8\ \mathrm{OH^-}$
R_3	$\mathrm{POM} + 2a\ \mathrm{MnO_2^{\alpha}} + 4a\ \mathrm{H^+} \rightarrow \mathrm{a}(1-f)\ {}^{12}\mathrm{CO_2} + af\ {}^{13}\mathrm{CO_2} + b\ \mathrm{NH_4^+} + c\ \mathrm{PO_4^{3-}} + 2a\ \mathrm{Mn^{2+}} + 3a\ \mathrm{H_2O}$
R_4	$\mathrm{POM} + 4a\ \mathrm{Fe(OH)_3^{\alpha}} + 4a\chi\ \mathrm{P_{ads}} \rightarrow a(1-f)\ {}^{12}\mathrm{CO_2} + af\ {}^{13}\mathrm{CO_2} + b\ \mathrm{NH_4^+} + (\mathrm{c} + 4\chi)\ \mathrm{PO_4^{3-}} + 3a\ \mathrm{H_2O} + 4a\ \mathrm{Fe^{2+}} + 8a\ \mathrm{OH^-}$
R_5	$\mathrm{POM} + 0.5a\ \mathrm{SO_4^{2-}} \rightarrow a(1-f)\ {}^{12}\mathrm{CO_2} + af\ {}^{13}\mathrm{CO_2} + b\ \mathrm{NH_4^+} + (\mathrm{c} + 4\chi)\ \mathrm{PO_4^{3-}} + 0.5a\ \mathrm{H_2S} + a\ \mathrm{OH^-}$
R_6	$\mathrm{NH_4^+} + 2\ \mathrm{O_2} + 2\ \mathrm{OH^-} \rightarrow \mathrm{NO_3^-} + 3\ \mathrm{H_2O}$
R_7	$\mathrm{Mn^{2+}} + 0.5\ \mathrm{O_2} + 2\ \mathrm{OH^-} \rightarrow \mathrm{MnO_2^{\alpha}} + \mathrm{H_2O}$
R_8	$\mathrm{Fe^{2+}} + 0.25\ \mathrm{O_2} + 2\ \mathrm{OH^-} + 0.5\ \mathrm{H_2O} + \chi\ \mathrm{PO_4^{3-}} \rightarrow \mathrm{Fe(OH)_3^{\alpha}} + \chi\ \mathrm{P_{ads}}$
R_9	$\mathrm{H_2S} + 2\ \mathrm{O_2} + 2\ \mathrm{OH^-} \rightarrow \mathrm{SO_4^{2-}} + 2\ \mathrm{H_2O}$
R_{10}	$\mathrm{FeS} + 2\ \mathrm{O_2} \rightarrow \mathrm{SO_4^{2-}} + \mathrm{Fe^{2+}}$
$R_{11}^{\alpha,\beta}$	$2\ \mathrm{Fe(OH)_3^{\alpha,\beta}} + 2\chi\ \mathrm{P_{ads}} + \mathrm{H_2S} \rightarrow 2\mathrm{Fe^{2+}} + 2\chi\ \mathrm{PO_4^{3-}} + \mathrm{S_0} + 4\ \mathrm{OH^-} + 2\ \mathrm{H_2O}$
$R_{12}^{\alpha,\beta}$	$\mathrm{MnO_2^{\alpha,\beta}} + 0.25\ \mathrm{H_2S} + 0.5\ \mathrm{H_2O} \rightarrow \mathrm{Mn^{2+}} + 0.25\ \mathrm{SO_4^{2-}} + 1.5\ \mathrm{OH^-}$
$R_{13}^{\alpha,\beta}$	$\mathrm{MnO_2^{\alpha,\beta}} + 2\ \mathrm{Fe^{2+}} + 2\chi\ \mathrm{PO_4^{3-}} + 2\ \mathrm{H_2O} + 2\ \mathrm{OH^-} \rightarrow 2\ \mathrm{Fe(OH)_3^{\alpha}} + 2\chi\ \mathrm{P_{ads}} + \mathrm{Mn^{2+}}$
R_{14}	$\mathrm{FeS} + \mathrm{S_0} \rightarrow \mathrm{FeS_2}$
R_{15}	$\mathrm{FeS_2} + 3.5\ \mathrm{O_2} + 2\ \mathrm{OH^-} \rightarrow 2\ \mathrm{SO_4^{2-}} + \mathrm{Fe^{2+}} + \mathrm{H_2O}$
R_{16}	$\mathrm{FeS} + 0.75\ \mathrm{H_2S} + 0.25\ \mathrm{SO_4^{2-}} \rightarrow \mathrm{FeS_2} + 0.5\ \mathrm{H_2O} + 0.5\ \mathrm{OH^-}$
R_{17}	$\mathrm{S_0} + 1.5\ \mathrm{O_2} + 2\ \mathrm{OH^-} \rightarrow \mathrm{SO_4^{2-}} + \mathrm{H_2O}$
$R_{18}^{\alpha,\beta}$	$3\ \mathrm{MnO_2^{\alpha,\beta}} + 2\ \mathrm{H_2O} + \mathrm{S_0} \rightarrow 3\ \mathrm{Mn^{2+}} + \mathrm{SO_4^{2-}} + 4\ \mathrm{OH^-}$
R_{19}	$\mathrm{MnO_2^{\alpha}} \rightarrow \mathrm{MnO_2^{\beta}}$
R_{20}	$\mathrm{Fe(OH)_3^{\alpha}} \rightarrow \mathrm{Fe(OH)_3^{\beta}}$
R_{21}^{+}	$\mathrm{Ca^{2+}} + (1-g)\ {}^{12}\mathrm{CO_2} + g\ {}^{13}\mathrm{CO_2} + 2\ \mathrm{OH^-} \rightarrow (1-g)\ \mathrm{Ca^{12}CO_3} + g\ {}^{13}\mathrm{CaCO_3} + \mathrm{H_2O}$
R_{21}^{-}	$(1-h)\ \mathrm{Ca^{12}CO_3} + h\ \mathrm{Ca^{13}CO_3} + \mathrm{H_2O} \rightarrow \mathrm{Ca^{2+}} + (1-h)\ {}^{12}\mathrm{CO_2} + h\ {}^{13}\mathrm{CO_2} + 2\ \mathrm{OH^-}$
R_{22}	$\mathrm{Fe^{2+}} + \mathrm{H_2S} + 2\mathrm{OH^-} \leftrightharpoons \mathrm{FeS} + 2\ \mathrm{H_2O}$

The stoichiometric parameters f, g, and h denote the $^{13}C/(^{12}C + {}^{13}C)$ fractions of POC, DIC, and TIC, respectively; P_{ads} and χ denote phosphate adsorbed to iron and the P:Fe adsorption ratio, respectively.

1159 Table 3: Rate expressions and kinetic rate constants

Rate expression	Rate parameters	Source[#]	Values source
Inhibition terms			
$I_{O2} = \frac{K_{m,O2}}{K_{m,O2}+[O_2]}$	$K_{m,O2} = 8$ µM	a	1-30
$I_{NO3} = \frac{K_{m,NO3}}{K_{m,NO3}+[NO_3]}$	$K_{m,NO3} = 12$ µM	a	4-80
$I_{MnO2} = \frac{K_{m,MnO2}}{K_{m,MnO2}+[MnO_2]}$	$K_{m,MnO2} = 4$ mmol kg^{-1}	a	4-32
$I_{Fe(OH)3} = \frac{K_{m,Fe(OH)3}}{K_{m,Fe(OH)3}+[Fe(OH)_3]}$	$K_{m,Fe(OH)3} = 65$ mmol kg^{-1}	a	65-100
Organic matter mineralization			
$R_1 = 10^2 k[POM](1 - I_{O2})$	$k = 0.06$ y^{-1}	m	
$R_2 = k[POM]I_{O2}(1 - I_{NO3})$			
$R_3 = k[POM]I_{O2}I_{NO3}$ $(1 - I_{MnO2})$			
$R_4 = k[POM]I_{O2}I_{NO3}$ $I_{MnO2}(1 - I_{Fe(OH)3})$			
$R_5 = k[POM]I_{O2}I_{NO3}$ $I_{MnO2}I_{Fe(OH)3}$			
Other reactions			
$R_6 = k_6[NH_4^+][O_2]$	$k_6 = 1.0 \times 10^4$ mM^{-1} y^{-1}	a	5e3-1e4
$R_7 = k_7[Mn^{2+}][O_2]$	$k_7 = 2.0 \times 10^4$ mM^{-1} y^{-1}	a	8e2-2e4
$R_8 = k_8[Fe^{2+}][O_2]$	$k_8 = 2.4 \times 10^6$ mM^{-1} y^{-1}	m	
$R_9 = k_9[H_2S][O_2]$	$k_9 = 1.0 \times 10^4$ mM^{-1} y^{-1}	a	≥ 160
$R_{10} = k_{10}[FeS][O_2]$	$k_{10} = 3.0 \times 10^2$ mM^{-1} y^{-1}	a	300
$R_{11} = k_{11}[Fe(OH)_3^{\alpha,\beta}][H_2S]$	$k_{11} = 2.0$ mM^{-1} y^{-1}	a	< 100
$R_{12}^{\alpha,\beta} = k_{12}[MnO_2^{\alpha,\beta}][H_2S]$	$k_{12} = 2.0$ mM^{-1} y^{-1}	a	< 10^5
$R_{13}^{\alpha,\beta} = k_{13}[MnO_2^{\alpha,\beta}][Fe^{2+}]$	$k_{13} = 2.0 \times 10^{-1}$ mM^{-1} y^{-1}	a	2
$R_{14} = k_{14}[FeS][S_0]$	$k_{14} = 1.0 \times 10^1$ mM^{-1} y^{-1}	a	7
$R_{15} = k_{15}[FeS_2][O_2]$	$k_{15} = 5.0 \times 10^2$ mM^{-1} y−1	m	
$R_{16} = k_{16}[FeS][H_2S]$	$k_{16} = 3.0$ mM^{-1} y^{-1}	m	
$R_{17} = k_{17}[S_0][O_2]$	$k_{17} = 1.0 \times 10^1$ mM^{-1} y^{-1}	m	
$R_{18}^{\alpha,\beta} = k_{18}[MnO_2^{\alpha,\beta}][S_0]$	$k_{18} = 3.0$ mM^{-1} y^{-1}	m	
$R_{19} = k_{19}[MnO_2^{\alpha}]$	$k_{19} = 6.0 \times 10^{-1}$ y^{-1}	a	1.8
$R_{20} = k_{20}[Fe(OH)_3^{\alpha}]$	$k_{20} = 2.0 \times 10^{-1}$ y^{-1}	a	0.6
Saturation state*			
$S_C = \frac{[Ca^{2+}][CO_3^{2-}]}{K_C} - 1$	$K_C = 2.1 \times 10^{-1}$ mM^2	b	
$S_S = \frac{[Fe^{2+}][HS^-]}{[H^+]K_S} - 1$	$K_S = 6.3 \times 10^1$ mM	m	

Mineral reactions†			
$R_{21}^{12,13} = \theta(S_C)k_{21}^{+}{S_C}^{12,13}f -$	k_{21}^{+}= 1.0 × 10^5 mM y^{-1}	c	10^5
$\theta(-S_C)k_{21}^{-}S_C[\mathrm{TI}^{12,13}\mathrm{C}]$	$k_{21}^{-} = 1.0\ y^{-1}$	c	5
$R_{22} = \theta(S_S)k_{22}^{+}S_S -$	k_{22}^{+}= 1.3 × 10^1 mM y^{-1}	m	
$\theta(-S_S)k_{22}^{-}[\mathrm{FeS}]$	$k_{22}^{-} = 1.0\ y^{-1}$	m	

[#]Sources: (a) Wang and Cappellen (1996), (b) Hofmann et al. (2010), (c) Luff and Wallmann (2003), (m) model constrained.

*[CO_3^{2-}] is the sum of [$^{12}CO_3^{2-}$] and [$^{13}CO_3^{2-}$].

[†]The θ function denotes the Heaviside step function. R_{21}^{12} and R_{21}^{13} implemented as separate reactions to distinguish turnover rates of ^{12}C and ^{13}C, respectively. ^{12}f and ^{13}f denote the fraction of light and heavy DIC, respectively.

Table 4: Boundary conditions

Chemical	Upper BC	Values
POM	F	37 g m^{-2} y^{-1}
MnO_2^{α}	ζ_0	0
	ζ_1	5.2×10^3 g m^{-3}
MnO_2^{β}	ζ_0	0
	ζ_1	5.2×10^3 g m^{-3}
$Fe(OH)_3^{\alpha}$	ζ_0	0.6 g m^{-2} y^{-1}
	ζ_1	1.0×10^4 g m^{-3}
$Fe(OH)_3^{\beta}$	F	0
$CaCO_3$	F	3.1 g m^{-2} y^{-1}
	$\delta^{13}C$	−2‰
FeS	F	0
FeS_2	F	0
S_0	F	0
O_2	C_0	150 µM
NO_3^-	C_0	23 µM
SO_4^{2-}	C_0	15 mM
Mn^{2+}	C_0	0
Fe^{2+}	C_0	0
H_2S	C_0	0
DIC	C_0	1.9 mM
	$\delta^{13}C$	−2‰
TA	C_0	1.9 mM
NH_4^+	C_0	0
PO_4^{3-}	C_0	0.5 µM
Ca^{2+}	C_0	5.7-6.7 mM

C_0 stands for fixed concentration boundary condition, and F stands for imposed flux. Upper boundary fluxes of MnO_2^{α}, MnO_2^{β}, and $Fe(OH)_3^{\alpha}$ are modeled as $F = \zeta_0 + (1 - \phi_0)w_0\zeta_1$, whereby ϕ_0 and w_0 are the porosity and burial velocity at the sediment-water interface, respectively. Zero-gradient boundary conditions are imposed at the bottom of the model domain.

Table 5: Transport parameters obtained by fitting porosity and mercury profiles.

Station		2_3	5_2	8_2	10_2	13_2	15_2	17_3	18_3
Sed. rate†	w_∞(mm y^{-1})	1.2	0.44	0.70	0.17	0.36	0.82	0.97	0.37
Turbation*	$\psi_0^{D_T}$(m^2 y^{-1})	32	32	32	32	32	32	32	32
	η^{D_T}(cm)	1.3	1.4	2.2	0.63	1.2	1.6	1.9	0.78
Porosity*	ψ_0^{ϕ}(%)	90	85	88	80	80	85	85	85
	ψ_∞^{ϕ}(%)	65	66	68	67	67	66	66	68
	η^{ϕ} (cm)	6.6	4.0	6.0	2.3	2.3	7.0	4.0	3.0

†The sediment accumulation rate is equivalent to the burial velocity below the compaction zone.

* See equation 3.

Figures

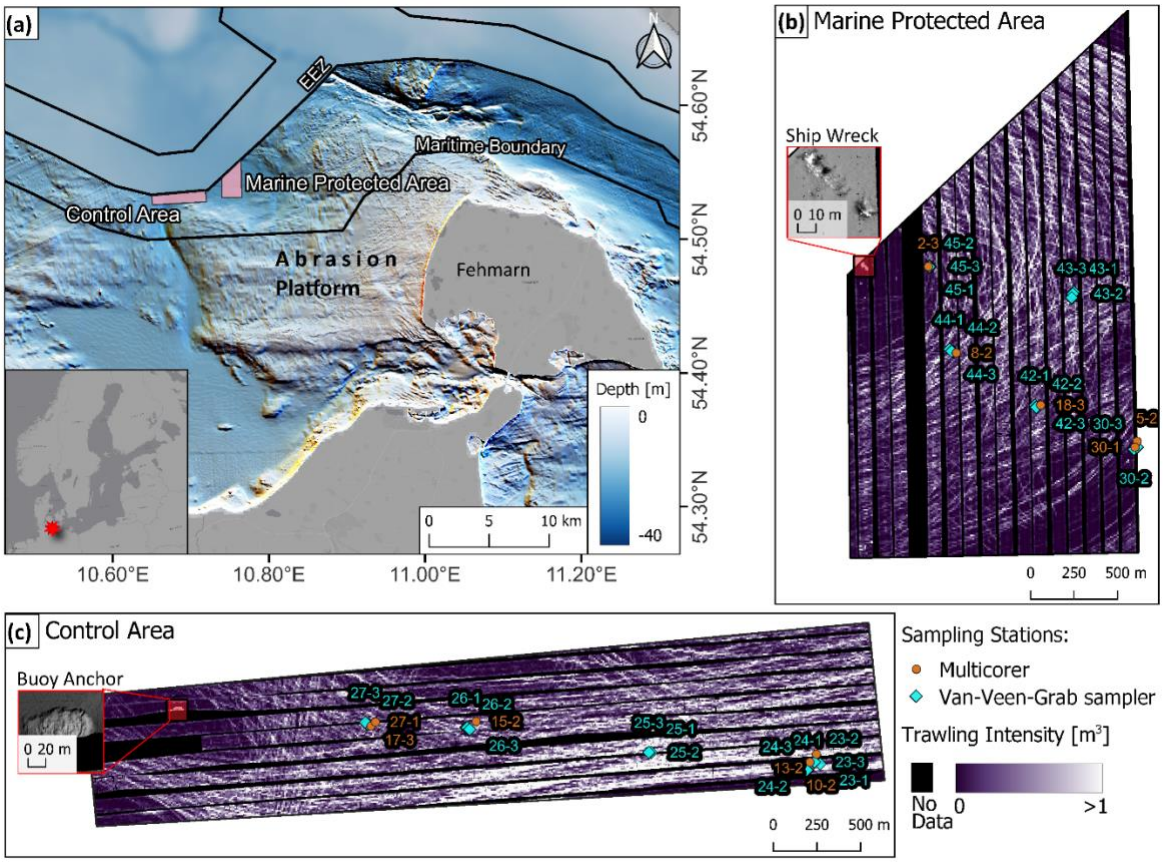

Figure 1: Bottom-trawling activity and coring locations in the study area. Panel (a) shows a bathymetric map offering an overview of the research areas in the Fehmarn Belt, all situated at a similar water depth. The control area's southern corner borders an abrasion platform, located east of the island of Fehmarn. Close-ups of highlighted focal areas are presented in panels (b) and (c). Trawl intensities, quantified as furrow volume per area, are color-coded, with light purple representing higher intensity and dark purple indicating lower intensity. Locations for Van-Veen-grab and multi-corer sampling (see legend) were calibrated using an ultra-short baseline (USBL) system. Bathymetry sources: Baltic Sea Hydrographic Commission (2013); Tauber (2012).

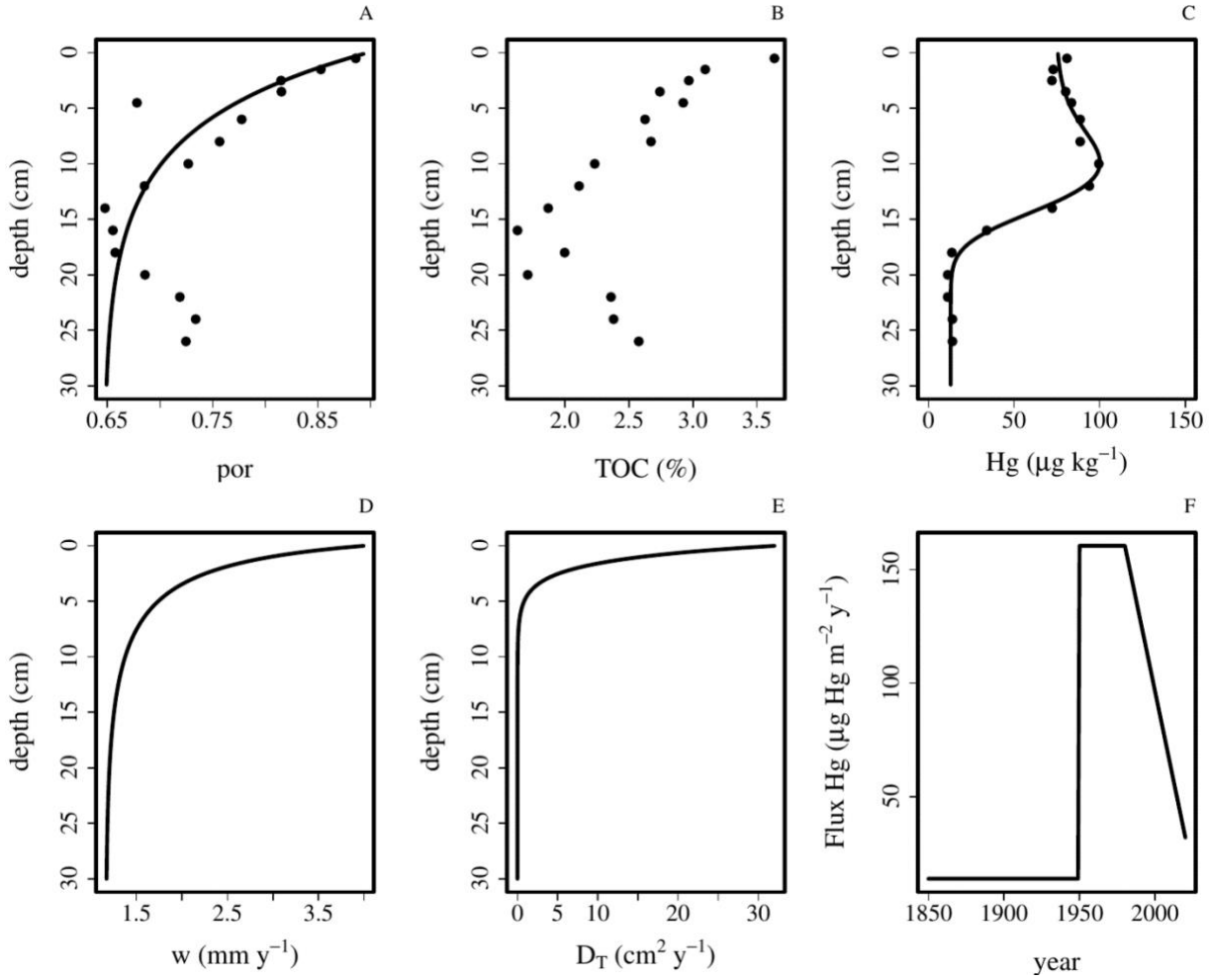

Figure 2: Constraining solid-phase transport for site 2_3 (dots are measurements, lines are model fits): (A) Porosity fitted with an exponential function, (B) The total organic carbon content, which correlates strongly with porosity (Spearman $r[14] = -.81$), (C) the mercury profile, which correlates weakly with total organic carbon content (Spearman $r[14] = .27$), (D) the burial velocity over depth, (E) the fitted turbation profile, (F) the Hg sediment loading (see text).

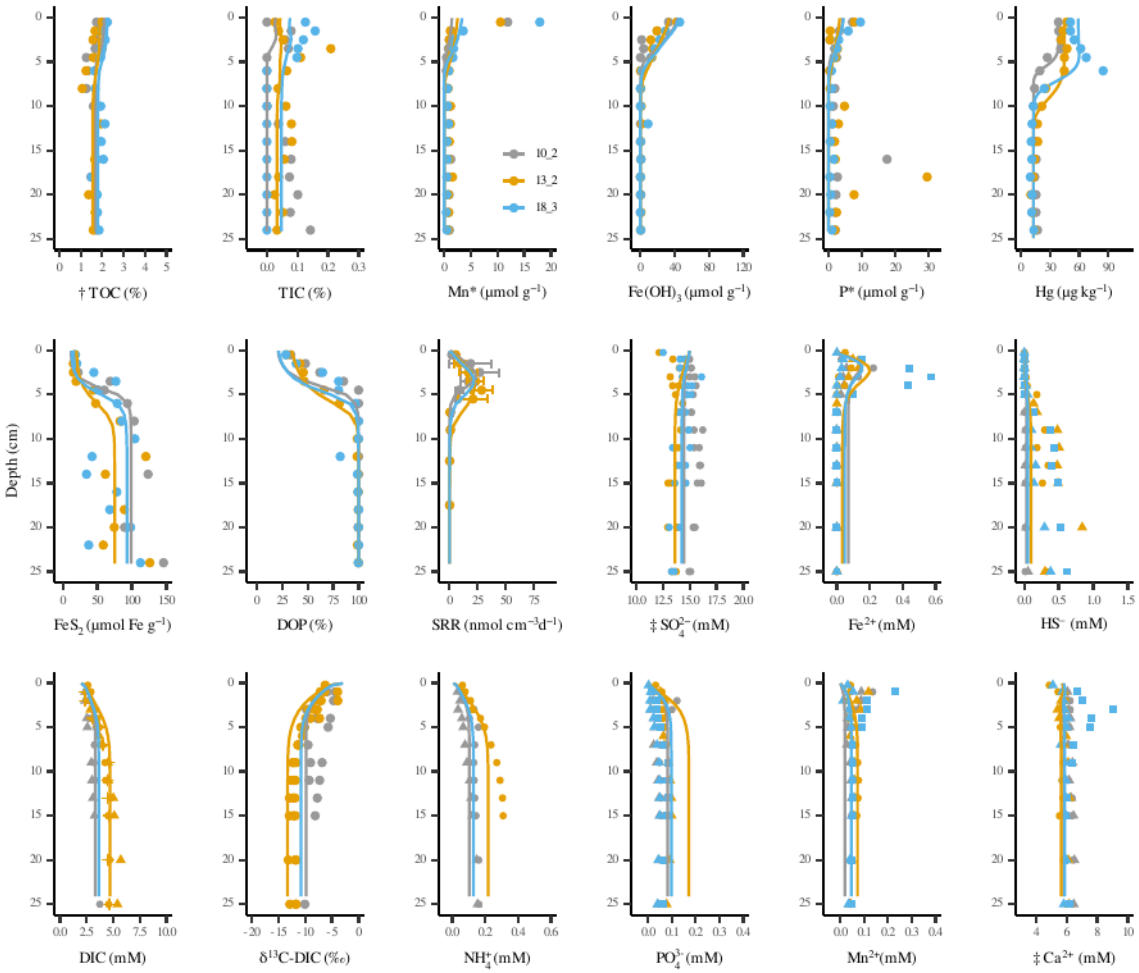

Figure 3: Comparison of simulated (bio-)geochemistry with measurements for three selected stations with slower solid-phase transport (Table 5). Distinct symbols are used to distinguish measurements from replicate sediment cores. The abbreviations DIC, SRR, and DOP represent dissolved inorganic carbon, sulfate reduction rate, and degree of pyritization, respectively. †The average measured TOC concentration below a depth of 15 cm was added to the simulated concentrations to account for refractory TOC not included in the model. ‡Measured SO_4^{2-} and Ca^{2+} concentrations were scaled to remove the trend associated with increasing salinity over depth.

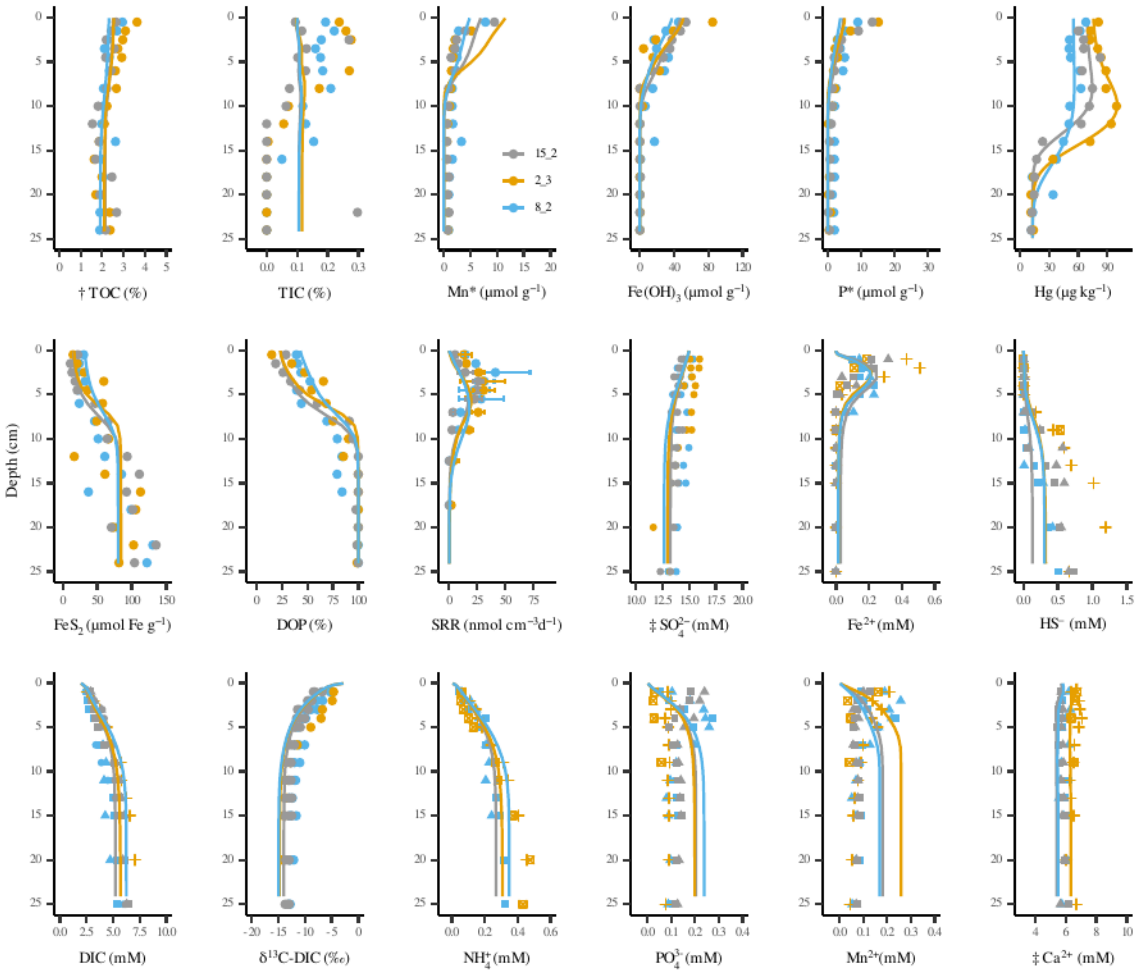

Figure 4: Comparison of simulated (bio-)geochemistry with measurements at three selected stations exhibiting faster solid-phase transport (Table 5). For symbol meanings and abbreviations, refer to Figure 3.

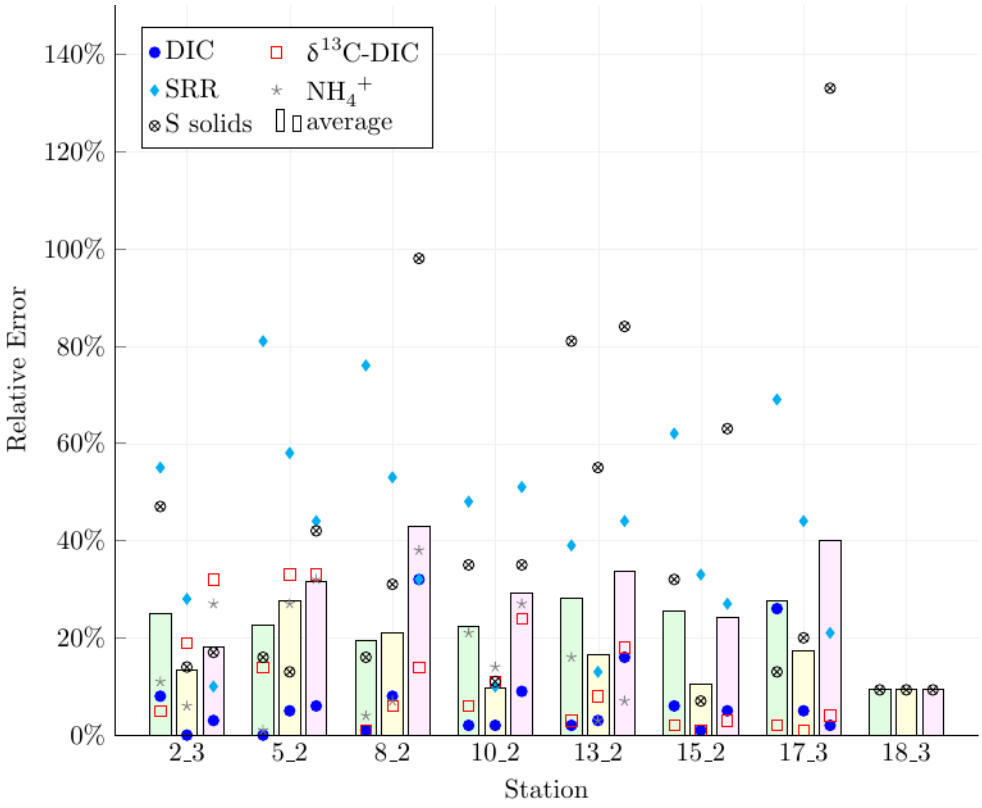

Figure 5: Sensitivity analysis for varying total reactive organic matter loading (F_{POM}) on model fits. Relative errors (eq. 6) of S solids, $Fe(OH)_3$, NH_4^+, SRR, DIC, and $\delta^{13}C$ are plotted with distinct symbols and colors (see legend). Bar heights represent the average error for these parameters. Each site's bars and symbols denote a 20% decrease (left, light green), no change (middle, light yellow), and a 20% increase (right, pink) in organic matter loading.

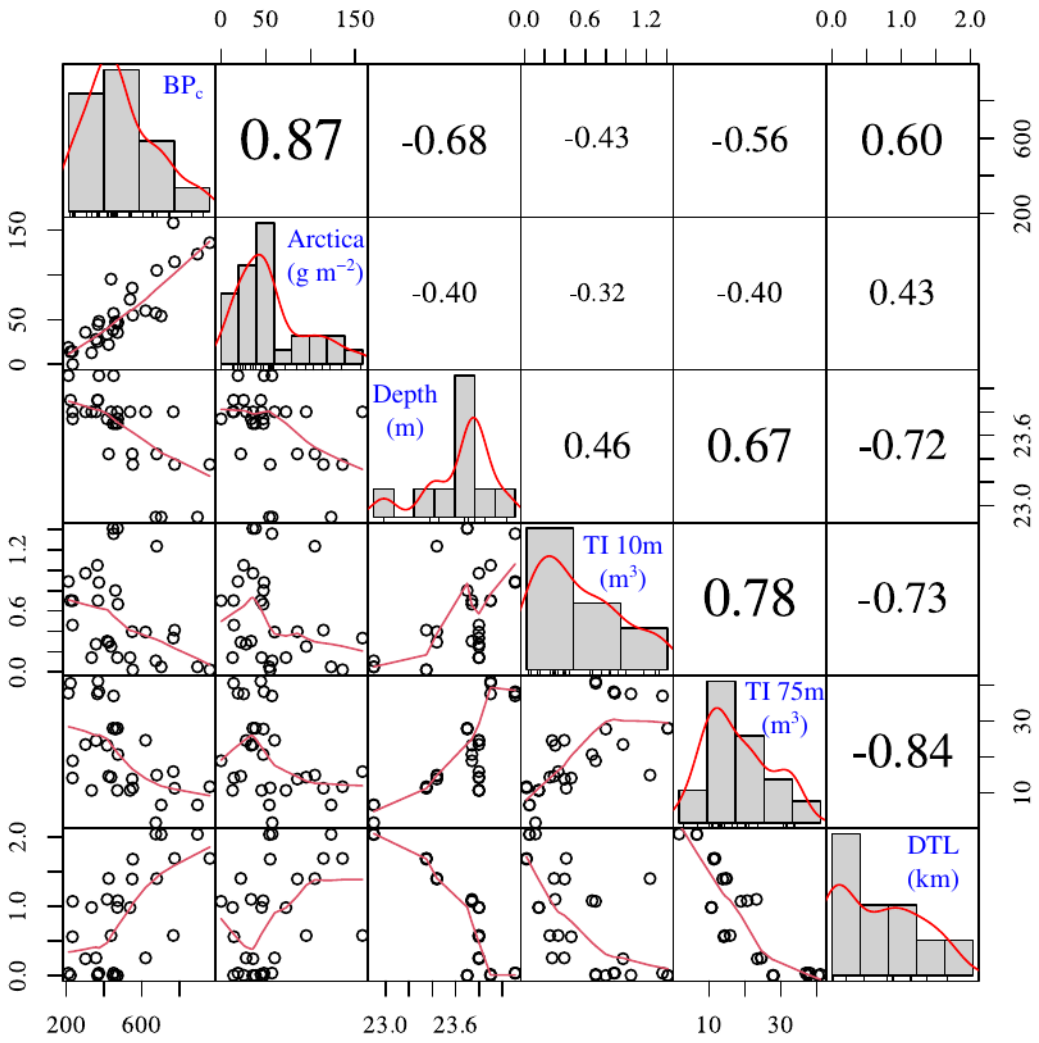

1219

1220 Figure 6: The Spearman correlations between bioturbation potentials (BP_c), *Arctica islandica*

1221 biomass, water-depth, trawling index based on furrow volume in 10 m x 10 m tiles (TI 10m) and

1222 75 m x 75m tiles (TI 75m), and distance from major trawling line (DTL).

1223

1224

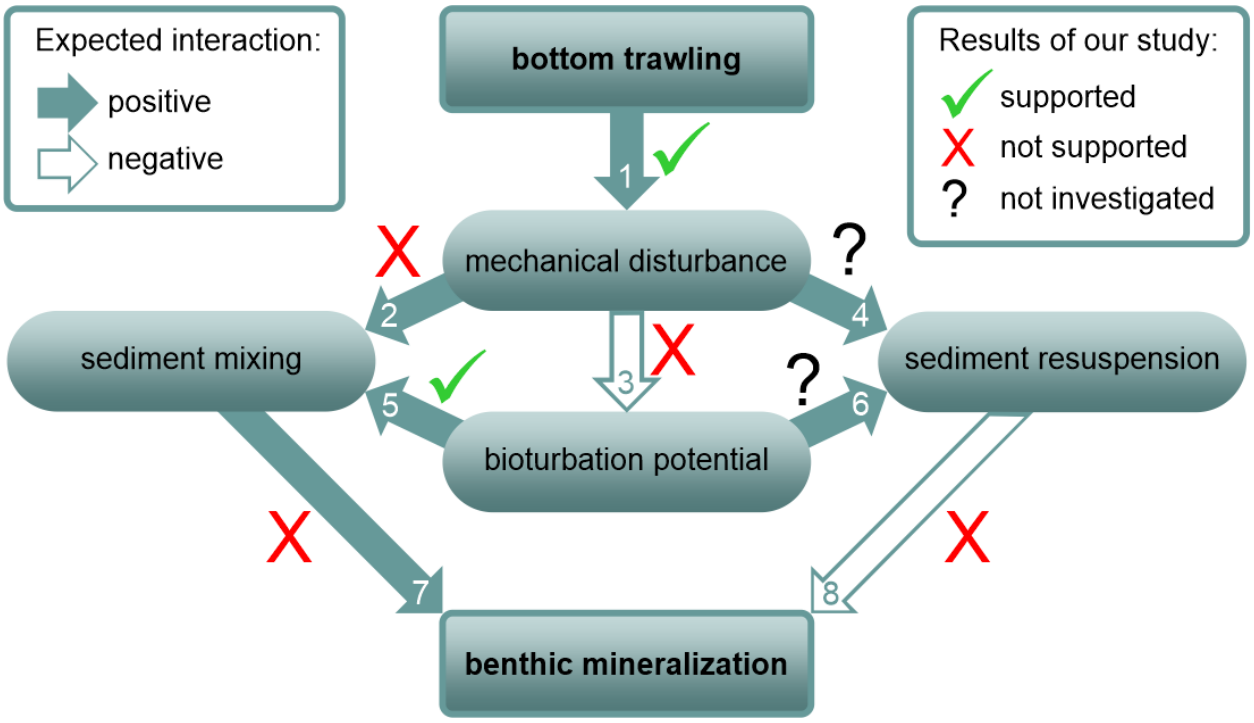

1225

1226 Figure 7: Main hypotheses for the effect of disturbances on early diagenesis (see text) and their

1227 relevance at the Fehmarn Belt.

1228

Effect of Bottom-Trawling on Early Diagenesis in the Southern Baltic Sea

Four facet approach

Mapped trawling activity

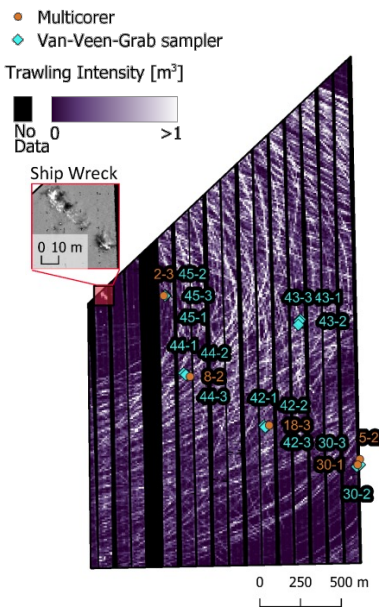

Biogeochemical data (BGC)

- solid-phase
- porewater

Arctica islandica

Macrofauna

- large, long-lived burrowers present despite trawling

Early diagenetic model

- depth-resolved reactive-transport
- calibrated on BGC
- 22 state variables
- bioturbation included

Main Findings

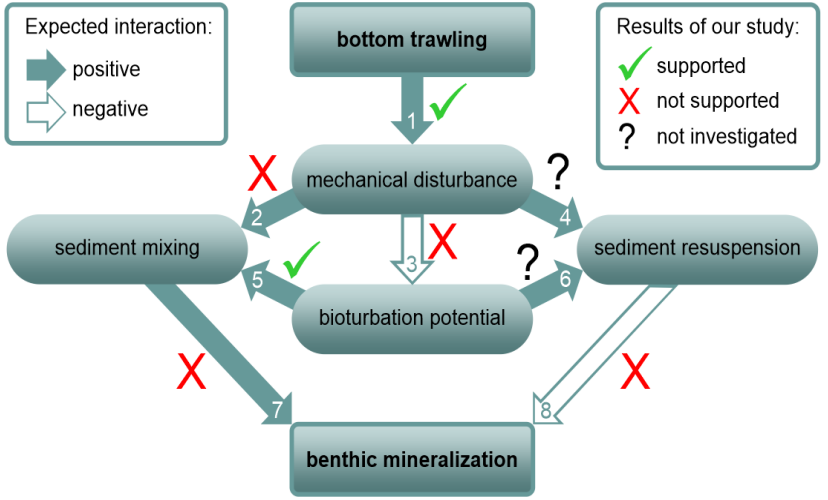

No clear impact of bottom-trawling on:
1) bioturbation potential
2) sediment mixing
3) organic matter mineralization
4) benthic carbon storage

The effects of bioturbation are stronger than the bottom-trawling disturbance

Supplementary Material

Jurjen Rooze, Mary A. Zeller, Mayya Gogina, Patricia Roeser, Jens Kallmeyer, Mischa Schönke, Hagen Radtke, Michael Ernst Böttcher

1. Supplementary Figure

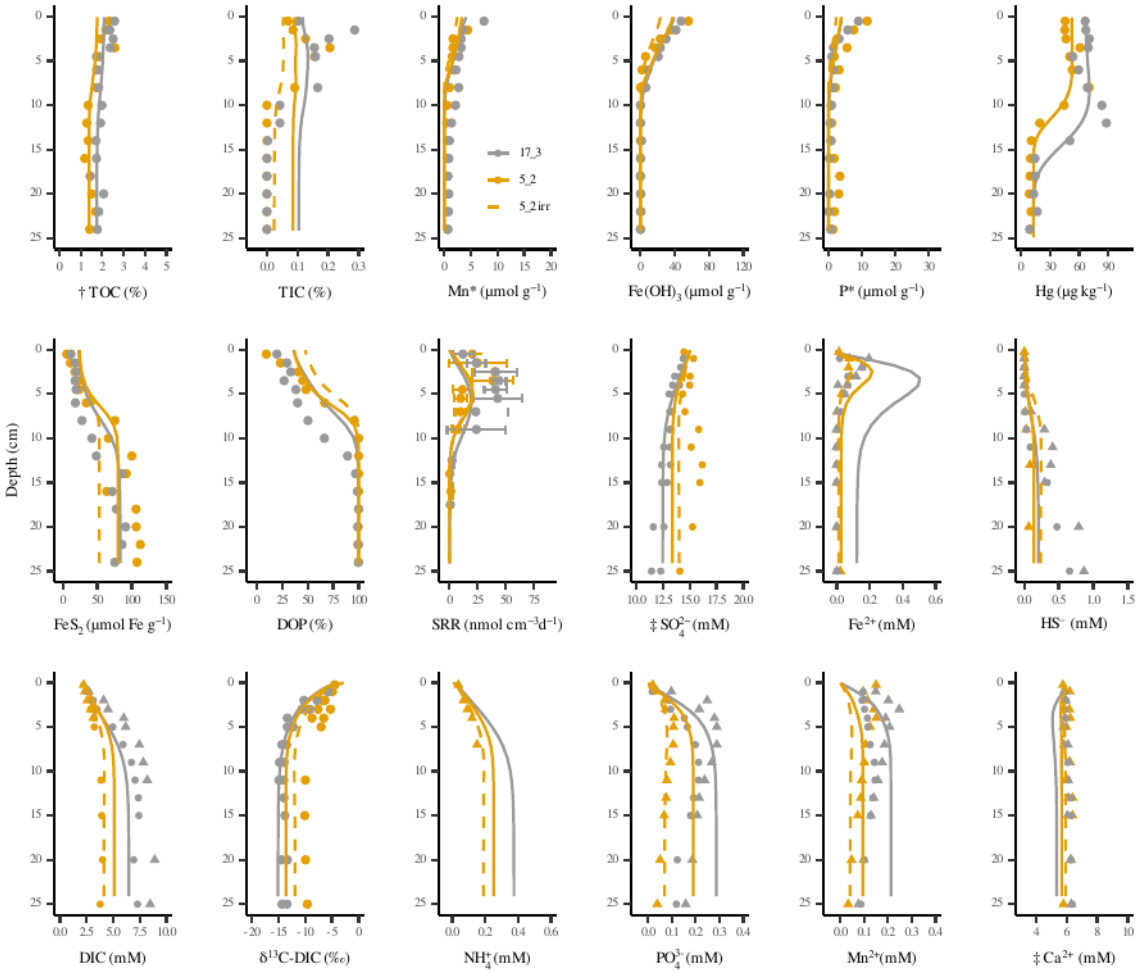

Figure S1: Simulated (bio-)geochemistry compared to measurements for sites 5_2 and 17_3. Dashed lines indicate the simulation for site 5_2 with bio-irrigation (5_2 irr) turned on. The measured sulfate reduction rates (SRR) come from the coring locations 5_4 (54°32.79' 10°46.62') and 17_2 (54°32.48' 10°41.18'). For the meaning of the symbols and abbreviations, refer to Figure 3 in the manuscript.

2. Supplementary Tables

Table S1: Sampling locations

Station	Latitude	Longitude	Water Depth (m)	Gear*	TI (m^3)†
2_3	54°33.35'	10°45.53'	23.0	MUC	0.00
5_2	54°32.8'	10°46.62'	23.4	MUC	
8_2	54°33.08'	10°45.67'	23.8	MUC	0.26
10_2	54°32.36'	10°43.48'	22.7	MUC	0.31
13_2	54°32.38'	10°43.52'	22.9	MUC	1.10
15_2	54°32.51'	10°41.72'	23.0	MUC	0.02
17_3	54°32.5'	10°41.16'	23.5	MUC	0.01
18_3	54°32.92'	10°46.11'	23.1	MUC	0.30
23_1	54°32.35'	10°43.53'	23.9	VVG	0.70
23_2	54°32.36'	10°43.5'	23.7	VVG	1.05
23_3	54°32.36'	10°43.5'	23.8	VVG	0.70
24_1	54°32.33'	10°43.47'	23.7	VVG	0.80
24_2	54°32.33'	10°43.47'	23.5	VVG	1.41
24_3	54°32.34'	10°43.46'	23.7	VVG	1.41
25_1	54°32.4'	10°42.64'	24.1	VVG	1.36
25_2	54°32.4'	10°42.63'	24.1	VVG	0.89
25_3	54°32.4'	10°42.63'	24.1	VVG	0.88
26_1	54°32.49'	10°41.67'	24.0	VVG	0.39
26_2	54°32.49'	10°41.67'	23.8	VVG	0.27
26_3	54°32.48'	10°41.68'	23.9	VVG	0.97
27_1	54°32.52'	10°41.19'	23.8	MUC	0.46
27_2	54°32.51'	10°41.14'	23.8	VVG	0.25
27_3	54°32.52'	10°41.13'	23.8	VVG	0.33
30_1	54°32.78'	10°46.61'	23.1	MUC	0.11
30_2	54°32.77'	10°46.6'	22.9	VVG	0.05
30_3	54°32.78'	10°46.62'	22.9	VVG	0.05
42_1	54°32.92'	10°46.08'	23.4	VVG	0.02
42_2	54°32.91'	10°46.09'	23.4	VVG	0.41
42_3	54°32.91'	10°46.09'	23.4	VVG	0.02
43_1	54°33.26'	10°46.3'	23.7	VVG	0.70
43_2	54°33.26'	10°46.3'	23.6	VVG	0.67
43_3	54°33.25'	10°46.29'	23.7	VVG	0.30
44_1	54°33.1'	10°45.63'	23.4	VVG	0.40
44_2	54°33.09'	10°45.65'	23.8	VVG	1.24
44_3	54°33.09'	10°45.64'	23.4	VVG	0.29
45_1	54°33.35'	10°45.54'	23.8	VVG	0.14
45_2	54°33.35'	10°45.54'	23.7	VVG	0.14
45_3	54°33.35'	10°45.54'	23.8	VVG	0.14

*MUC and VVG stand for multicorer and Van Veen Grab sampler, respectively. †TI stands for trawling index based on furrow volume in 10 m x 10 m tiles.

Table S2: Taxa dominating abundance and biomass (ash-free dry weight, AFDW) and mean values of these parameters in the study area. Frequency indicates the percentage of occurrence of taxa in all 30 grab samples (15 grab samples each in MPA and control area).

Taxa	Abundance (ind. m^{-2})	Frequency (%)	Taxa	AFDW biomass (g m^{-2})	Frequency (%)
Ophiura albida	198	100	*Arctica islandica*	56.08	100
Varicorbula gibba	190	100	*Nephtys ciliata*	2.12	100
Diastylis rathkei	183	97	*Ophiura albida*	0.68	100
Abra alba	139	90	*Asterias rubens*	0.34	3
Scoloplos armiger	123	100	*Abra alba*	0.20	90
Levinsenia gracilis	79	100	*Phaxas pellucidus*	0.15	67
Nephtys ciliata	73	100	*Diastylis rathkei*	0.07	97
Arctica islandica	43	100	*Lagis koreni*	0.07	83
Aricidea suecica	32	93	*Terebellides stroemii*	0.06	43
Lagis koreni	27	83	*Scoloplos armiger*	0.06	100
Phaxas pellucidus	18	67	*Varicorbula gibba*	0.04	100
Kurtiella bidentata	17	77	*Psammechinus miliaris*	0.04	3
Terebellides stroemii	14	43	*Malacobdella grossa*	0.03	30
Paradoneis eliasoni	11	50	*Lineus ruber*	0.02	3
Tubificinae	9	47	*Philine aperta*	0.02	30
Phoronis sp.	8	47	*Tritia reticulata*	0.01	17
Halcampa duodecimcirrata	8	53	*Levinsenia gracilis*	0.01	100
Peringia ulvae	7	37	*Aricidea suecica*	0.01	93
Ampharete baltica	6	47	*Rhodine loveni*	0.01	23
Gastrosaccus spinifer	5	37	*Halcampa duodecimcirrata*	0.01	20
Prionospio steenstrupi	4	30	*Nucula nitidosa*	0.01	53
Total abundance	1226 (±388)		Total biomass	60(±27)	